JACS
JOURNAL OF THE AMERICAN CHEMICAL SOCIETY
Article
Cite This: J. Am. Chem. Soc. 2019, 141, 9837−9853
pubs.acs.org/JACS

Structure and Function in Antimicrobial Piscidins: Histidine Position, Directionality of Membrane Insertion, and pH-Dependent Permeabilization

Mihaela Mihailescu,[*,†] Mirco Sorci,[‡] Jolita Seckute,[§] Vitalii I. Silin,[†] Janet Hammer,[∥] B. Scott Perrin, Jr.,[⊥] Jorge I. Hernandez,[#] Nedzada Smajic,[▽] Akritee Shrestha,[▽] Kimberly A. Bogardus,[▽] Alexander I. Greenwood,[■] Riqiang Fu,[○] Jack Blazyk,[∥] Richard W. Pastor,[⊥] Linda K. Nicholson,[§] Georges Belfort,[*,‡] and Myriam L. Cotten[*,■]

[†]Institute for Bioscience and Biotechnology Research, University of Maryland, Rockville, Maryland 20850, United States
[‡]Department of Chemical and Biological Engineering and Center for Biotechnology and Interdisciplinary Studies, Rensselaer Polytechnic Institute, Troy, New York 12180, United States
[§]Department of Molecular Biology and Genetics, Cornell University, Ithaca, New York 14853, United States
[∥]Department of Biomedical Sciences, Ohio University, Athens, Ohio 45701, United States
[⊥]Laboratory of Computational Biology, National Heart, Lung, and Blood Institute, National Institutes of Health, Bethesda, Maryland 20892, United States
[#]Department of Bioengineering, Clemson University, Clemson, South Carolina 29634, United States
[▽]Department of Chemistry, Hamilton College, Clinton, New York 13323, United States
[■]Department of Applied Science, College of William and Mary, Williamsburg, Virginia 23185, United States
[○]National High Magnetic Field Laboratory, Tallahassee, Florida 32310, United States

Supporting Information

ABSTRACT: Piscidins are histidine-enriched antimicrobial peptides that interact with lipid bilayers as amphipathic α-helices. Their activity at acidic and basic pH in vivo makes them promising templates for biomedical applications. This study focuses on p1 and p3, both 22-residue-long piscidins with 68% sequence identity. They share three histidines (H3, H4, and H11), but p1, which is significantly more permeabilizing, has a fourth histidine (H17). This study investigates how variations in amphipathic character associated with histidines affect the permeabilization properties of p1 and p3. First, we show that the permeabilization ability of p3, but not p1, is strongly inhibited at pH 6.0 when the conserved histidines are partially charged and H17 is predominantly neutral. Second, our neutron diffraction measurements performed at low water content and neutral pH indicate that the average conformation of p1 is highly tilted, with its C-terminus extending into the opposite leaflet. In contrast, p3 is surface bound with its N-terminal end tilted toward the bilayer interior. The deeper membrane insertion of p1 correlates with its behavior at full hydration: an enhanced ability to tilt, bury its histidines and C-terminus, induce membrane thinning and defects, and alter membrane conductance and viscoelastic properties. Furthermore, its pH-resiliency relates to the neutral state favored by H17. Overall, these results provide mechanistic insights into how differences in the histidine content and amphipathicity of peptides can elicit different directionality of membrane insertion and pH-dependent permeabilization. This work features complementary methods, including dye leakage assays, NMR-monitored titrations, X-ray and neutron diffraction, oriented CD, molecular dynamics, electrochemical impedance spectroscopy, surface plasmon resonance, and quartz crystal microbalance with dissipation.

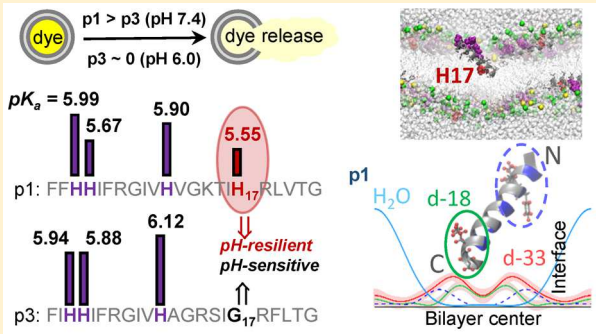

INTRODUCTION

The amphipathic α-helix (AH) is a structural motif employed by membrane-interacting peptides and proteins to mediate vital processes that require membrane remodeling, such as cell fusion, entry, and lysis.[1−6] A perfect AH has a strict segregation of its hydrophilic and hydrophobic residues and a ratio of hydrophilic to hydrophobic area of 1.0 (equivalently, a "polar angle" of 180°). As such, it complements the chemistry of the water−bilayer interface and binds parallel to the bilayer

Received: January 13, 2019
Published: May 30, 2019

DOI: 10.1021/jacs.9b00440
J. Am. Chem. Soc. 2019, 141, 9837−9853

Table 1. List of Methods and Sample Conditions Used on p1 and p3

method	lipids	configuration	P/L	[P] in μM[a]
dye leakage	3:1 POPC:POPG	LUVs	1:256−1:2	
NMR titration	3:1 PC:PG[b]	bicelles	1:20	
	SDS, DPC	micelles	1:100	
MD simulations	3:1 POPC:POPG	BL	1:20	
			1:40	
OCD	3:1 POPC:POPG	BL	1:150−1:8	
ND	3:1 POPC:POPG	BL	1:25−1:16	
			1:25	
			1:12	
X-ray	3:1 POPC:POPG	BL	1:134−1:16	
solid-state NMR	3:1 POPC:POPG	BL	1:80	
SPR	3:1 POPC:POPG	tBL		3
				2.5−20
QCM-D	3:1 POPC:POPG	tBL		2−20
				11.4

[a]Concentrations of the peptide solutions flown on the supported bilayers are indicated for the surface-sensitive techniques. [b]Bicelles were made using a 3:1 molar ratio between the long chains 14-0-PC and 14-O-PG (see Materials and Methods). BL = bilayer; tBL = tethered bilayer.

surface, with the nonpolar side chains interacting with the lipid acyl chains and hydrophilic residues pointing toward the polar lipid headgroups.[7] Notably, membrane-binding AHs that are biologically active usually feature some degree of imbalance in their amphipathicity, including polar angles different from 180°, charged residues present on the nonpolar face, N- and C-terminal ends with unequal numbers of charged residues, and hydrophilic faces enriched in one type of residue.[2,5,6,8] Such imperfections affect the relative magnitude of the electrostatic and hydrophobic interactions between AHs and bilayers. However, it is not well understood how specific imperfections influence the membrane conformations and/or orientations ("topologies") and functions of AHs.

As one of the most studied classes of AHs, cationic α-helical antimicrobial peptides (AMPs) exhibit permeabilization and/or cell-penetrating properties. They rely on positive charges to enhance their electrostatic interactions with anionic bacterial membranes and selectively target bacteria over host cells.[9−13] Basic arginines and lysines are their primary sources of cationicity. Histidines, which are pH-responsive in the physiological pH range, can also contribute to cationicity if the pH and environment favor their protonated state. Direct killing of bacteria by AMPs is most commonly attributed to damaged plasma membranes, leading to various effects, such as membrane blebbing, permeabilization, and depolarization.[8,10,14−17] In some cases, membrane-active AMPs employ cell-penetrating rather than permeabilizing properties to kill cells: after translocating across cell membranes, they damage intracellular targets.[16,18,19]

Permeabilizing amphipathic peptides disrupt membranes in a concentration-dependent manner.[14,20−25] AMPs, which tend to have polar angles near 180°, bind parallel to the membrane surface (S-state) at low concentrations (peptide-to-lipid ratio, P/L < 1:500).[26,27] Permeabilization of large solutes typically appears once a critical P/L* is reached and leakage-competent states are established in the membrane through a process that involves reorienting peptides from the S-state to a tilted state that either partially or fully crosses the membrane. The structures of the permeabilizing states remain uncertain. In the pore view, "pore-forming peptides" adopt fixed transmembrane (TM) oligomeric structures filled with water. In the case of nonselective peptide toxins, strong evidence indicates that their amphipathically imperfect AHs associate to form toroidal "lipidic" pores even at low P/L (<1:1000). These pores feature merged lipid monolayers due to the recruitment of lipid headgroups to stabilize a TM state of the AH where the cationic side chains are inserted in the hydrocarbon core.[21,23,28,29]

Direct evidence for TM pores is lacking for a large number of AHs, many of which are membrane-active AMPs.[8,14,25,30−32] Nonpore mechanisms have been suggested to explain why their vesicle leakage behavior is often slow, transient, and dependent on membrane composition and high P/L (>1:500).[8,30,31] For instance, the "interfacial activity" model proposes that "defect-inducing peptides" abolish the structural integrity of the membrane by desegregating its polar and nonpolar regions as the peptides transiently cross membranes to equilibrate their concentrations on each side of the membrane.[8] This mechanism stipulates that amphipathic imperfections enhance bilayer disordering albeit at the cost of lower cell specificity.[8,31] Recent all-atom molecular dynamics (MD) simulations have indicated that AMPs form metastable pores or pore-like defects that elude experimental methods due to their transient nature and heterogeneous structural features.[33−36]

We recently identified significant differences in permeabilization strengths between piscidin 1 (p1, FFHHIFRGIVHVGKTIHRLVTG) and piscidin 3 (p3, FIHHIFRGIVHAGRSIGRFLTG), two homologous and α-helical AMPs from fish.[16,37−42] The peptides are differentially expressed, with p3, the less hemolytic isoform, more preponderant in vascularized tissues.[41,43,44] Although they are both efficacious AMPs (e.g., respective minimum inhibitory concentrations of 4 and 8 μM on *Escherichia coli*) and have cell-penetrating properties that allow them to exist on both sides of bacterial membranes, p1 is 3−4-fold more effective at permeabilizing bacterial and model membranes.[16,45] It also kills bacteria within minutes as compared to 1 h for p3, possibly because the mechanism of p3 requires entering cells to disrupt DNA.[16,37] Structurally, they share three histidines in their N-terminal halves, and p1 has an extra histidine in the C-terminal region, H17. Bound to membranes, they adopt similar structures, but H17 creates an amphipathic imperfection due to its position at the polar−nonpolar interface of the AH.[38]

DOI: 10.1021/jacs.9b00440
J. Am. Chem. Soc. 2019, 141, 9837−9853

In vivo, multiple piscidins are deployed during bacterial infections. They kill bacteria at both basic (extracellularly) and acidic (phagosomes) pH values.[43,46,47] Thus, piscidins, collectively or individually, feature pH-resiliency (i.e., retain similar function across a broad pH range) despite being distinctively rich in histidines (14−20% in p1 and p3 versus 2% on average in other AMPs).[48] In contrast to AMPs that lose their charge and activity at basic pH because they rely primarily on histidines for cationicity, piscidins remain cationic in the physiological pH range due to multiple arginines and lysines.[49] However, it is unclear how the charge state of their histidines affects their permeabilization strength and pH-sensitivity.

In this study, we investigated the effects of pH on the permeabilization strengths of p1 and p3, and the structures of each peptide and surrounding membrane. By comparing two homologous AHs that have cell penetrating properties but differ significantly in permeabilizing effects, our goal was to examine how variations in amphipathic character associated with histidines affect their bilayer interactions, topologies, and permeabilization properties. Because they share amphipathicity, cationicity, and α-helicity with other AHs and differences in histidine content yield distinctive amphipathic imperfections, p1 and p3 are good archetypes for studying the relationships between the amphipathic and permeabilization properties of AHs.

Given that biological membranes exhibit complex physicochemical properties, rigorous biophysical studies of membrane-bound peptides and proteins require selecting a model membrane system that promotes native-like molecular behaviors.[50−57] In this research, we favored phospholipid bilayers and bicelles to reproduce membrane characteristics (e.g., the lateral pressure profile and 2-order magnitude change in dielectric constant across the membrane) known to affect peptide structures and molecular interactions.

We subjected p1 and p3 to complementary methods (Table 1) and compared their behavior in terms of charge, permeabilization strength and pH-resiliency, bilayer structure and interaction, and ability to alter membrane conductance and viscoelastic properties. Specifically, we used vesicle leakage assays at acidic and basic pH values, and NMR-monitored titrations in lipid bicelles, to investigate how the membrane activities of p1 and p3 are affected by the charge of their histidines. We performed molecular dynamics (MD) simulations on surface-bound p1 and p3 to determine the insertion depths of their histidines and employed surface-sensitive methods to characterize their effects on membrane conductance and viscoelastic properties. We supplemented these studies with structural investigations by neutron diffraction (ND), in conjunction with specific deuterium labeling of the peptides, lipids, and water. This allowed us to examine the positions and orientations of p1 and p3 simultaneously with the structures of the surrounding bilayer and water, as needed to connect our macroscopic observations and molecular-level structural data. The structural work used conditions where p1 and p3 differed significantly in membrane reorientation, permeabilization, and thinning capabilities, based on oriented CD (OCD), leakage, and X-ray diffraction data. MD simulations provided insights into the dynamic structural ensemble adopted by the peptides in the bilayer. Altogether, this study shows that peptides differing in histidine content and amphipathic imperfection in their C-terminal regions can exhibit contrasted directionalities of membrane insertion, permeabilization strengths, and pH-behaviors.

MATERIALS AND METHODS

Materials, Peptide Synthesis, and Purification. Unless otherwise specified, chemicals were purchased from Millipore Sigma (Saint Louis, MO). Carboxyamidated p1 (MW 2571) and p3 (MW 2492) were chemically synthesized at the University of Texas Southwestern Medical Center and purified on a Waters HPLC system with a C18 column and acetonitrile/water gradient, as previously reported.[38,41] The ^{2}H-labeled forms of the peptides used in the ND experiments (d18-p1 = L19d$_{10}$V20d$_8$, d15-p3 = F19d$_5$L20d$_{10}$, d33-p1 = I5d$_{10}$F6d$_5$L19d$_{10}$V20d$_8$, and d30-p3 = I5d$_{10}$F6d$_5$F19d$_5$L20d$_{10}$) were similarly synthesized. The labeled amino acids were obtained from Cambridge Isotope Laboratories (Tewksbury, MA). After lyophilization, the peptides were dissolved in dilute HCl and dialyzed to remove residual trifluoroacetic acid, leading to 98% pure peptides. Following reconstitution of the peptides in nanopure water, their molar concentrations were determined by amino acid analysis performed at the Protein Chemistry Center at Texas A&M. The stocks were diluted in buffer, as needed for the different experiments. Phospholipids were purchased from Avanti Polar Lipids (Alabaster, AL). Fresh solutions were made in chloroform, and concentrations were determined by solution NMR using trioxane as an internal reference.

Calcein Leakage from Large Unilamellar Vesicles (LUVs) Treated with Piscidin. The ability of p1 and p3 to induce leakage in membranes was estimated by monitoring the rate of fluorescence enhancement when calcein-loaded LUVs were exposed to the AMPs. LUVs contained 4 μmol (total lipid) of 3:1 (mol:mol) 1-palmitoyl-2-oleoyl-*sn*-glycero-3-phosphocholine/1-palmitoyl-2-oleoyl-*sn*-glycero-3-phosphoglycerol (POPC/POPG). The experiments were performed following a protocol previously published and summarized in the Supporting Information.[16]

Solution NMR Titration of the Histidine Side Chains of p1 and p3. The histidine side chains of p1 and p3 were reconstituted in three chemical environments, as described in the Supporting Information: 3:1 phosphocholine/phosphoglycerol (PC/PG) isotropic bicelles as well as dodecylphosphocholine (DPC) and sodium dodecyl sulfate (SDS) micelles. Piscidin samples containing a single ^{15}N-labeled histidine residue at position 3, 4, 11, or 17 of p1, or 3, 4, or 11 of p3, were subjected to pH titration by solution NMR at 298 K in the presence of the bicelles and micelles. Progress of the titrations was monitored using previously established heteronuclear multiple quantum coherence solution NMR experiments and described in the Supporting Information.[58,59]

To calculate the pK_a of each ^{15}N-labeled imidazole side chain, the chemical shifts of its ε1 proton were plotted as a function of pH and fitted to the following equation using the least-squares method:

$$\delta(\mathrm{pH}) = \frac{\delta\mathrm{His}^+ + \delta\mathrm{His}^0 \times 10^{\mathrm{pH}-\mathrm{p}K_a}}{1 + 10^{\mathrm{pH}-\mathrm{p}K_a}} \quad (1)$$

where δ(pH) is the proton chemical shift of the ε1 proton at a given pH, δHis$^+$ and δHis^0 are the chemical shifts for the positively charged (His$^+$) and neutral (His^0) states, respectively, and pK_a is the pH at which one-half of the titrating group is protonated.[59] The pK_a value for each plot was obtained through a process of minimizing the root-mean-square deviation (rmsd) between observed and calculated chemical shifts. For the titrations in SDS micelles, the ^{15}N chemical shifts were also fitted and yielded pK_a values in agreement with those determined from ^{1}H chemical shifts (standard deviation, SD $\leq$ 0.10), indicating that ^{1}H chemical shifts could be reliably used to obtain pK_a values within 0.10 units. Representative plots are shown in Figure S1.

Molecular Dynamics (MD) Simulations. The dependence of histidine charge state and peptide insertion depth was determined from 100 ns simulations of p1 in 3:1 POPC/POPG with 1 peptide and 40 lipids per leaflet (P/L = 1:40). Values for all neutral histidines were obtained from our previously reported[60] simulations, and additional trajectories at two different charge states were generated for this study (Table S2). The prior work included pressure profiles. Initial peptide structures were generated with φ/ψ angles of −61° and −45°, respectively, and extended side chains. Peptides were aligned

DOI: 10.1021/jacs.9b00440
J. Am. Chem. Soc. 2019, 141, 9837−9853

with their centers of mass (COM) 14 Å above or below the center of the bilayer and hydrophobic residues facing the bilayer core. Simulations were performed with CHARMM 38b2,[61] the CHARMM 36 protein force field,[62] the CHARMM 36 lipid force field[63] with corrections for sodium binding,[64] and the TIP3P water model,[65,66] and contained approximately 50 waters/lipid (see the Supporting Information for more details).

The simulations described above contained only 1 peptide per leaflet and were run for 100 ns. While this is sufficient to generate reliable average insertion depths for peptides at low concentration, the system sizes are too small, the trajectories too short, and the peptides too isolated to analyze excursions to the midplane and defects at the conditions of many of the experiments reported here. Consequently, a previously published[33] trajectory of 8 p1 peptides per leaflet at P/L = 1:20 and 56 waters/lipid was extended to 3.0 μs. A comparable simulation of p3 in 3:1 POPC/POPG was carried out for 0.4 μs. These simulations were used to calculate the depth distributions of the histidine side chains. Potentials of mean force (PMF) were calculated from these distributions $p(z)$ as $\mathrm{PMF}(z) = -RT \ln p(z)$, where R is the gas constant, and T is temperature.

Oriented Circular Dichroism (OCD). Samples were prepared as previously reported.[16,41,42] Briefly, a 3:1 POPC/POPC mixture (approximately 0.5 mg) dissolved in chloroform was combined with a desired quantity of p1 or p3 in 2,2,2-trifluoroethanol. After evaporation of the solvents under a flow of nitrogen, each sample was placed under vacuum for at least 8 h before being hydrated, vortexed, and spread on a quartz slide. The sample was then equilibrated overnight at 298 K before being placed in a sealed stainless wheel that contained a saturated K_2SO_4 solution (~98% relative humidity). Following equilibration for two hours, CD spectra were obtained at eight angles (i.e., every 45°) using a Jasco J-815 spectrometer (Jasco Analytical Instruments, Easton, MD). The data were collected at 298 K between 190 and 260 nm with a 100 nm/min scan speed of 1 nm bandwidth, and signal averaging over 4 scans. Artifacts from linear dichroism were avoided by spreading the samples in a thin layer over a surface area that was about 10 mm in diameter and averaging the spectra collected at eight different angles. A blank sample containing 3:1 POPC/POPG but no piscidin was recorded and subtracted from the signal obtained in the presence of piscidin.

Neutron Diffraction (ND). Oriented lipid multilayers with piscidins were prepared as above using 1.5−2 mg of lipids (3:1 POPC/POPG) per sample. After removal of the organic solvents, the lipid/peptide mixtures were thoroughly hydrated with water at neutral pH and fused on thin glass coverslips allowing the bulk water to slowly evaporate at room temperature. The resulting oriented lipid (lamellar) samples were annealed at 98% relative humidity and 303 K for at least 12 h before measurements. Hydrated lamellar samples containing 2000−3000 bilayers with piscidins in either protonated or deuterated form were measured under controlled temperature−humidity conditions (296 ± 0.5 K, 86% and 93% relative humidities) on the MAGIk instrument at the National Institute of Standards and Technology (NIST) Center for Neutron Research, Gaithersburg, MD.

Bragg diffraction probing the axis perpendicular to the bilayer plane (z-axis) was used to determine the one-dimensional scattering length density (SLD) profile of the bilayer. Up to five Bragg diffraction peaks (h = 1−5) were observed (Figure S2) for each of the measured samples, with the peaks h = 1−3 being the most prominent. Bilayer structure factors (Tables S3 and S4) were obtained as the square root of the integrated Bragg peaks, corrected for background, absorption, and extinction, and their phases determined by deuterium contrast, using $H_2O/^2H_2O$ exchange.[67−69] The bilayer one-dimensional SLD profile was calculated by Fourier synthesis of the structure factors. All profiles were determined on a per-lipid "absolute-relative" scale using structure factors calibrated to reflect the composition of the unit cell and without explicitly determining the area per lipid.[68] The contrasts between deuterium-containing and natural abundance samples arising from the higher neutron scattering length of deuterium ($b^2H = 6.67 \times 10^{-5}$ Å) with respect to hydrogen ($bH = -3.74 \times 10^{-5}$ Å) were used to parse out by difference the SLD profiles of the deuterated regions. For p3, the composition-based scale of the profiles was determined, to the best approximation, using the deuterium peaks of the N- and C-termini for the calibration. For samples containing p1, because profiles were noisier, an additional, homologous sample containing the deuterated lipid 1-palmitoyl-2-oleoyl-sn-glycero-3-phosphocholine-1-1-2-2-d4-*N*,*N*,*N*-trimethyl-d9 (d13-POPC) was used as a standard for calibration (Figure S3). The thus calibrated SLD profiles were also used to determine the amount of water per lipid headgroup, as described previously.[70] Briefly, the conformations (position and orientation) of p1 and p3 in the bilayer were parametrized by fitting the measured deuterium difference structure factors (Δf) with Gaussian models, as described previously.[70] A Levenberg−Marquardt nonlinear least-squares fit was used, with χ^2 weighted by the uncertainties in the measured data (SD, due to counting statistics). Fit parameter confidence intervals were determined by a Monte Carlo resampling technique,[68,71] where a large number (n = 100) of statistically independent sets of mock structure factor values (normally distributed within ±1 SD) were tested, thus producing one set of fit parameters for each iteration. Means and SDs of the fit parameters were calculated from these sets.

Surface Plasmon Resonance/Electrochemical Impedance Spectroscopy (SPR/EIS) Measurements on Tethered Bilayer Lipid Membranes (tBLMs). SPR/EIS experiments were conducted using a custom-built SPR instrument. The specifications of the instrument[72] and the methodology used to form tBLMs[73,74] are briefly described in the Supporting Information. The freshly prepared tBLMs (Figure S4A) were equilibrated in HEPES buffer (50 mmol/L HEPES, 50 mmol/L NaCl, pH 7.4) and allowed to rest until SPR and EIS signals stabilized (30−40 min). Solutions of p1 and p3 in HEPES buffer were then introduced into the tBLM-containing SPR/EIS cell to a final concentration of 3 μmol/L. After 10 min of incubation, the cell was rinsed with the buffer, and the SPR/EIS measurements were continued for another 10 min.

Intensity distribution versus pixel position on the camera chip was measured by SPR. The pixel positions of the SPR minima corresponding to minimum reflectivity were plotted as a function of time. EIS data were recorded from 1 to 10 kHz at a rate of 1 spectrum per minute, resulting in a total 22 spectra for each experiment. Each spectrum contained 100 data points. The Z-plot and Z-view software (Scribner Associates, Inc., NC) was employed for the impedance spectral collection and analysis. The simplest electrical circuit model (Figure S4B) was used to fit the impedance data using a complex nonlinear least-squares minimization procedure based on a Levenberg−Marquardt algorithm implemented in the Zview software. The SD in the fit parameters (e.g., capacitance and resistance) were estimated from the residuals of the fit (mean square error).

Quartz Crystal Microbalance with Dissipation (QCM-D) on Supported Lipid Bilayers (SLBs). QCM-D runs were performed at 296 K in Tris buffer (10 mmol/L, 100 mmol/L NaCl, pH 7.4) using an E4 auto system and its standard flow module QFM 401 (Biolin Scientific/Q-Sense, Linthicum, MD). Polished silicon dioxide quartz crystals with fundamental frequencies of ~5 MHz (QSX 303, Biolin Scientific/Q-Sense, Linthicum, MD) were washed with Milli-Q water, rinsed with ethanol, and dried with N_2. Organic contaminants were removed by plasma cleaning (Atomflo 400L2 Plasma System, Surfx Technologies, Culver City, CA) at 120 W (30 L/min He, 0.2 L/min O_2) for 4 min. Crystals were used immediately after plasma cleaning. SLBs were formed following the protocol by Cho et al.[75] Specifically, 3:1 POPC/POPG SLBs were made following a two-step process: (i) fast adsorption and (ii) rupture of the small unilamellar vesicles (SUVs) on the silicon dioxide surface. The preparation of the SUVs is described in the Supporting Information. A buffer wash was performed for an additional 10 min, to allow complete SLB annealing as described by Briand et al.[76] At this point, the AMP was flown onto the SLB. In the initial experimental setup, the QCM-D pump was then stopped, and the SLB was incubated with the peptide solution for up to 1 h. Because having an incubation step did not affect the values of Δf and ΔD in the subsequent steps (e.g., the 15 min buffer wash), all experiments were performed using a continuous flow mode. Each run ended with thorough cleaning of the silica surface using a

DOI: 10.1021/jacs.9b00440
J. Am. Chem. Soc. 2019, 141, 9837−9853

2% SDS solution and washing it with buffer until the baseline stabilized. Runs were done at a crossflow rate of 100 μL/min. The data were analyzed using a well-established procedure summarized in the Supporting Information.

^{2}H Solid-State NMR Experiments, X-ray Diffraction Data Collection, and Membrane Binding Kinetics Measurements by SPR on Biacore Chips. These experiments are described in the Supporting Information.

RESULTS

Dye Leakage: Membrane Permeabilization Potencies of p1 and p3 as a Function of pH. Our prior results showed that p1 is more permeabilizing to bacterial membranes than p3.[16] Because the lipid mixture 3:1 POPC/POPG has been widely used to mimic bacterial cell membranes, we used it to compare the membrane permeabilization strength and pH-resiliency of p1 and p3. We prepared 3:1 POPC/POPG LUVs containing trapped calcein and measured how much fluorescent dye is released when each AMP is added at a specific concentration (Figure 1). We chose the pH values of 6.0 and 7.4 to reflect conditions experienced by the peptides in vivo.

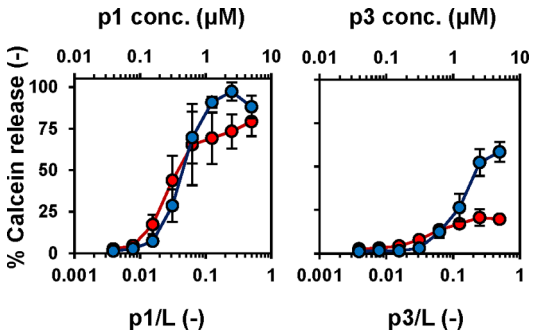

Figure 1. Permeabilization assays on 3:1 POPC/POPG vesicles exposed to p1 and p3. The % calcein release (mean ± SD) is plotted as a function of p1 (left) and p3 (right) concentration for at least six measurements (n = 6) done at pH 7.4 (blue) and pH 6.0 (red).

Both peptides display the typical behavior of AMPs: beyond a given threshold concentration, leakage increases in a sigmoidal fashion, reflecting the cooperativity of the permeabilization process.[77] While both p1 and p3 induce leakage from the LUVs at pH 6.0 and 7.4, p1 is significantly more effective than p3 at both pH values. In particular, in terms of maximum permeabilization capability, p1 is equally effective at pH 6.0 and 7.4 within the 95% confidence level, that is, within 2 SDs (97 ± 6% and 79 ± 9% at pH 7.4 and 6.0, respectively), while p3 is much weaker at pH 6.0 than at 7.4 (58 ± 6% and 20 ± 2% at pH 7.4 and 6.0, respectively). Furthermore, the peptide concentrations yielding 50% leakage (EC_{50}) are lower for p1 than p3. At pH 7.4, the EC_{50} values are p1/L = 1:22 = 0.045 (0.45 μmol/L) and p3/L = 1:4 = 0.25 (2.5 μmol/L). At pH 6.0, p1 has an EC_{50} value of P/L = 1:20 = 0.05 (0.50 μmol/L), while p3 is too weak to have an EC_{50}. Overall, the dye leakage experiments ascertain that 3:1 POPC/POPG is a reliable system to capture the stronger membrane activity of p1 as compared to p3. Importantly, the results also reveal that p1 is more pH-resilient than p3 in the 6.0−7.4 window.

NMR-Monitored Titrations: Determination of Peptide Charge in the Physiological pH Range Using the pK_a Values of the Individual Histidine Side Chains Present in p1 and p3. To determine whether the contrasted membrane activities and pH-behaviors of p1 and p3 originate from different peptide charges as a function of pH and peptide identity, we determined the charges of p1 and p3 at both pH 6.0 and 7.4. Ionizable groups in p1 and p3 include the side chains of the basic residues (Arg, Lys, and His) and the N-terminus. Because arginine and lysine side chains have high pK_a's, they can readily be assumed to have the same positive charge in p1 and p3, and at pH 6.0 and 7.4. Given that p1 and p3 have highly conserved N-terminal sequences and the average pK_a of the N-terminus in proteins is 7.7,[78] we reasoned that the N-terminal charge of each piscidin is +1 at pH 6.0 and 7.4. However, histidine side chains have an average pK_a of 6.5[79] and are pH-responsive in the physiological range, and thus determine any change in the overall charge of p1 and p3 as the pH changes from 6.0 to 7.4. Because the exact pK_a of histidine is highly sensitive to its local environment and we wanted to accurately characterize the overall charge of each peptide, we deemed it necessary to determine the pK_a of each histidine side chain in p1 and p3. For this purpose, we performed NMR-monitored pH titrations for each side chain when each peptide was bound to 3:1 PC/PG. More specifically, piscidin peptides containing a single ^{15}N-labeled histidine side chain were titrated in the presence of 3:1 PC/PG isotropic bicelles. We used a P/L of 1:20 and C14:0 acyl chains, which were previously shown by solid-state NMR and MD to stabilize to the S-state of piscidin.[38,60]

Table 2. pK_a Values for the Histidine Side Chains of p1 and p3 Bound to 3:1 PC/PG Bicelles[a,b]

		pK_a (± 0.10)			
		H3	H4	H11	H17
3:1 PC/PG bicelles	p1	5.99	5.67	5.90	5.55
	p3	5.94	5.88	6.12	N/A

[a]The SD for the pK_a values is ± 0.10, as determined from titrations using both ^{15}N and ^{1}H chemical shifts. [b]Representative NMR data and titrations curves are shown in Figure S1.

In bicellar solutions, the peptides are in exchange between bound and unbound states. Therefore, it is important to establish that the state detected by NMR is the bound form of interest for the titrations. Previous studies of p1 by Campagna et al. and Lee et al. in SDS and DPC micelles, respectively, ascertained that the α-helical bound state was detected.[80,81] Given that these earlier studies provided useful benchmarks to demonstrate that the solution NMR signals arise from the bound state of the peptide, we also reconstituted and titrated p1 and p3 in the presence of SDS and DPC micelles. However, we note that micellar systems have limitations that may lead to inaccurate determination of structures and molecular interactions,[82] and thus only the titration results from the bicellar samples were relied upon to determine peptide charge. Several features of our NMR titration data on p1 and p3 confirmed that the signals observed were arising from the bound state: (i) we detected broadening and upfield shifts of the α-proton signals, as previously reported by Campagna et al. and Lee et al.;[80,81] (ii) we observed major differences in pK_a values when labeled peptides were pH-titrated in different biomembrane mimetic environments (e.g., PC/PG bicelles, and SDS and DPC micelles (Table 2 and Table S1)); (iii) the pH titration curves could be readily fitted with small rmsd (≤ 0.07); and (iv) the dissociation rate proved to be slow relative to the association rate on the NMR time scale because a separate set of peaks for free and bound were not detected (this assumes

DOI: 10.1021/jacs.9b00440
J. Am. Chem. Soc. 2019, 141, 9837−9853

that the chemical differences between free and bound states of the observed histidines are larger than the peak line width of several Hz). This was confirmed in membrane-binding kinetics experiments by SPR (Figure S5 and Table S5).

NMR-monitored titration plots in 3:1 PC/PG bicelles showing the change of $\varepsilon 1$ proton chemical shifts of the ^{15}N-labeled histidine chain versus pH are displayed in Figure 2, and

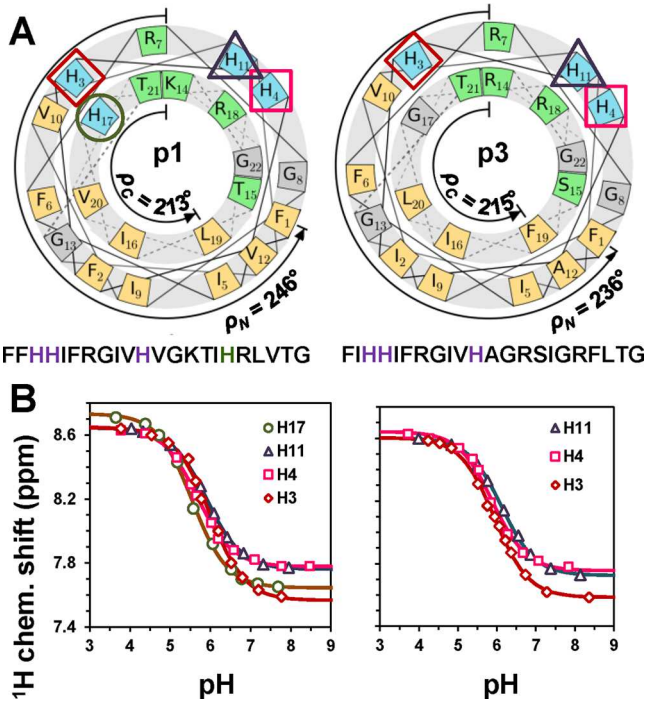

Figure 2. Determination of peptide charge via NMR-monitored titrations of the histidine side chains of p1 and p3 bound to PC/PG bicelles. (A) Color-coded helical wheels and amino sequences of p1 (left) and p3 (right), based on previously determined structures.[38] The shared histidines are indicated in purple, and H17 is in green. (B) NMR-monitored titration curves for p1 and p3 in the bilayer. Each histidine is marked a specific colored symbol (e.g., red square). The chemical shifts of $H^{\varepsilon 1}$ in the imidazole ring of each histidine were followed as a function of pH, and the resulting curve was fitted to the Henderson–Hasselbalch equation to obtain the pK_a value of the corresponding histidine side chain in situ (see Materials and Methods).

the pK_a values obtained from fitting the chemical shifts versus pH plots using eq 1 are summarized in Table 2. For each p1 (p3), there are four (three) plots, each corresponding to one of the four (three) histidines. The pK_a values are between 5.55 ± 0.1 and 6.12 ± 0.10; therefore, the histidine side chains of p1 and p3 are completely neutral at pH 7.4, while at pH 6.0 they carry a partial positive charge, and thus make the peptides more cationic at pH 6.0 than 7.4. We note that H4 and H17 have the lowest pK_a values (5.67 and 5.55, respectively) of the seven histidines, suggesting that their environments are the most nonpolar.

With an average pK_a of 5.77 in p1 versus 5.98 in p3, the histidines of p1 are only 37% charged at pH 6.0, while those of p3 are 49% charged. Scaled up to 4 and 3 histidine residues in p1 and p3, respectively, this small (12%) difference in charge shows that, although p1 carries one more histidine than p3, it is not more charged at pH 6.0. Thus, p1 has, within experimental error, the same charge as p3 not only at pH 7.4 when the histidines are neutral ($Q_{p1} = Q_{p3} = +4.0 \pm 0.1$), but also at pH 6.0 when these side chains are partially charged ($Q_{p1} = +5.3 \pm 0.1$ and $Q_{p3} = +5.4 \pm 0.1$).

The titration results lead to two important conclusions. First, combined with the dye leakage data, they show that the permeabilization effects of p3, but not p1, require that the conserved histidines be neutral. Second, the histidine side chains of p1 have overall lower pK_a values than those of p3, enabling p1 to have the same charge as p3 even at acidic pH. Thus, charge alone does not explain the stronger permeabilization strength and pH-resiliency of p1 revealed in the dye leakage experiments. Because their hydrophobicities[45] and hydrophobic moments[38] (Table S6) are also comparable, they cannot account for the different permeabilization behaviors either.

MD Simulations: Insertion Depths and Defects. The titration experiments indicated that the four histidines of p1 have overall lower pK_a values than the three histidines of p3 when the peptides are in the S-state. This begged the question as to whether the histidine side chains of p1 reach more deeply in the hydrophobic core of the bilayer than those of p3. Table 3 lists the average insertion depths of each histidine with

Table 3. Insertion Depths[a] with Standard Errors (Å) for Individual Histidines of p1 and p3 at P/L = 1:20; Root Mean Squared Fluctuations (Å) in Parentheses

histidine	p1	p3
H3	2.9 ± 0.1 (2.7)	2.3 ± 0.1 (2.3)
H4	4.5 ± 0.1 (2.9)	2.9 ± 0.1 (2.4)
H11	4.0 ± 0.1 (2.8)	2.4 ± 0.1 (2.4)
H17	4.5 ± 0.1 (3.5)	N/A

[a]Each reported depth corresponds to the distance along the membrane normal between the COM of the specified histidines and the instantaneous average of all lipid phosphorus atoms.

respect to the phosphate plane from simulation systems containing 8 peptides per leaflet with P/L = 1:20, and neutral histidines. The histidines of p1 insert more deeply than those of p3, with H4 and H17 adopting an equilibrium position approximately 4.5 Å below the phosphorus atoms while the histidine side chains of p3 do not insert deeper than 2.9 Å.

The peptides are highly dynamic, and the root mean squared fluctuations (in parentheses in Table 3) are comparable to the mean insertion depths. Hence, averages are best used to understand trends and not to be interpreted as precise locations in the membrane. To this end, Figure S6 plots the distributions of insertion depths of the COM of the individual histidines of p1 and p3 with respect to the midplane. Excursions to the midplane are also more energetically favorable for p1 than for p3, as is evident from the potentials of mean force (PMF) plotted in Figure 3. Of particular note, the potential energy penalty for sampling the midplane ($z = 0$) is only 3 kcal/mol for H17 of p1. With the H17 side chain strongly populating a nonpolar environment of the bilayer, its neutral state is stabilized, thereby explaining its particularly low pK_a (Table 2). It is also evident from the distributions (but less so the means) that deep insertions into the bilayer are more favorable for the C-terminal (red line showing H17) of p1, while p3 shows a mild preference for N-terminal insertion (blue line showing H3).

Figure S7 plots the positions of H3 and H17 for each of the 16 p1 peptides over the 3 μs trajectory, and includes snapshots

DOI: 10.1021/jacs.9b00440
J. Am. Chem. Soc. 2019, 141, 9837–9853

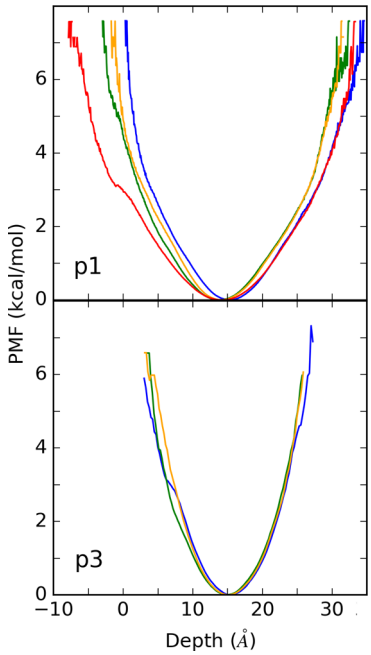

Figure 3. Potentials of mean force for p1 and p3 in 3:1 POPC/POPG. Coloring is as follows for p1 (top) and p3 (bottom): His 3 (blue), His 4 (green), His 11 (yellow), and His 17 (red). Averages are over 16 peptides at P/L = 1:20, and z = 0 specifies the average position of the bilayer midplane. The phosphate plane is at approximately 19 Å.

of the bilayer at 0.9, 1.9, and 2.8 μs. There were 20 excursions of H17 to within $z = \pm 5$ Å of the midplane over the 3 μs trajectory for the 16 peptides, for an average of 0.4 per peptide per μs. H3 (near the N-terminal), in contrast, only had a single entry into the $z = \pm 5$ Å band. From the PMFs of p1 (Figure 3), the free energy difference between H17 and H3 at z = 5 is 1 kcal/mol. The ratio of excursions can then be estimated to be $\exp(\Delta G/RT) \approx 5$. This estimate is more robust than that obtained directly from the preceding counts, where the statistical uncertainty is quite high. The third snapshot in Figure S7 shows a substantial undulation of the membrane at 2.8 μs. Homogenous bilayers of this size, an edge-length of 10 nm, do not exhibit such large undulations,[83] indicating that the distortion is peptide-generated.

Figure 4 focuses on the 1.9 μs snapshot, where three peptides on one leaflet cooperatively tilted into the bilayer and produced a conical water-filled half-channel. This defect, which is formed by the C-termini of two peptides and the N-terminal of a third, is closely associated with two POPG headgroups, and stable for only approximately 100 ns. The defect at 0.9 μs pictured in Figure S7 involves a deeply inserted C-terminus interacting with a somewhat less inserted N-terminus in the same leaflet. A third example of a defect involving p1 was observed in a previously published trajectory initialized with 20 p1 peptides arranged in 4 barrel-stave pores.[33] In this case, 18 of the 20 TM peptides migrated to the surface by 15 μs, and a defect involving the N- and C-termini of two peptides on the same leaflet formed at 19.8 μs. Hence, all three of the defects observed in our simulations of p1 involved both N- and C-termini of different peptides. While the waters are mostly confined to the one leaflet, the cone-shape defects do facilitate water leakage through the bilayer; in this sense, the defects might be described as "funnel-like".

The 0.4 μs trajectory of 16 p3 peptides did not show large undulations or defects. Given that defect formation is on the microsecond time scale for conventional MD simulations carried out at physiological temperatures, longer simulations or enhanced sampling methods will be required to more fully characterize defects induced by p3 and study the translocation events for both peptides.

As was already noted, the peptides can also induce transient undulations in the bilayer (e.g., the 2.8 μs snapshot in Figure S7). This underscores why it was important to analyze the defects described above with respect to the local, not the global, bilayer midplane. Nevertheless, average insertion depths from 100 ns simulations of systems with only 4 peptides per 80 lipids (2 per leaflet, P/L = 1:20) differ by only 0.1 Å from those in Table 3 (data not shown), indicating that undulations present in the larger system (8 peptides per leaflet) do not substantially change the mean depths.

Last, we explored the effects of protonating H17, the histidine present in p1 but absent in p3, on the insertion depth

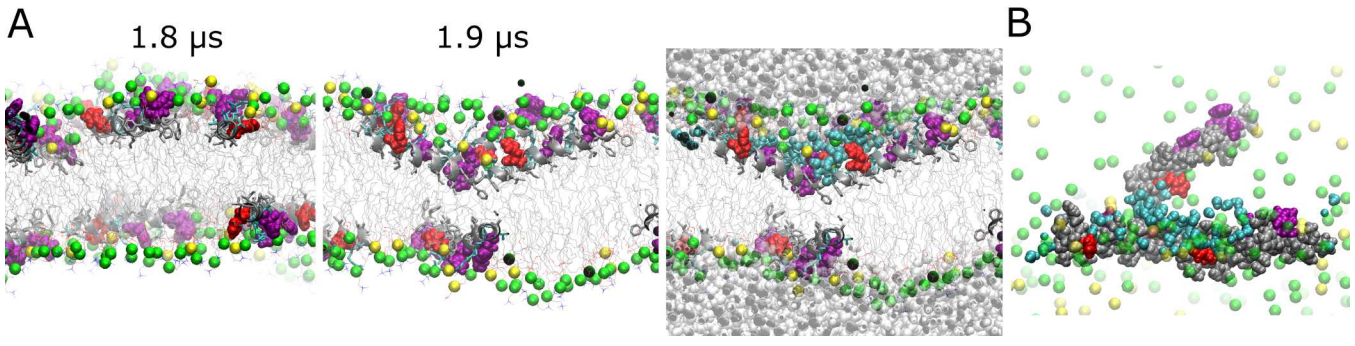

Figure 4. Defect from a 3 μs trajectory of 16 p1 in a 3:1 POPC/POPG bilayer at P/L = 1:20. (A) Side views. The left panel (1.8 μs) shows a typical configuration with the peptides close to the equilibrium insertion depths. The middle panel (1.9 μs) captures a transient "funnel-like" defect in the top leaflet where two p1's have inserted their C-terminal ends in the bilayer, bringing their H17 side chains in close proximity to interact with the H3 and H4 side chains from the N-terminus of a third peptide. The right panel includes waters within 10 Å of the midplane for the 1.9 μs frame. Water atoms, when present, are rendered as cyan spheres when within 10 Å of the midplane and gray otherwise. Other components are displayed as follows: peptide backbones (gray ribbons); histidine side chains (space-filling with H17 in red, and H3, H4, and H11 in purple); remaining peptide side chains (sticks); POPC and POPG phosphates (green and yellow spheres, respectively); and remaining lipid atoms (light gray sticks). (B) Top down, slightly tilted, view of the 1.9 μs configuration with associated waters. Coloring is the same as in (A), except nonhistidine residues are in space-filling gray spheres while peptides not in the defect and nonphosphate lipid atoms are removed for clarity.

DOI: 10.1021/jacs.9b00440
J. Am. Chem. Soc. 2019, 141, 9837−9853

of p1 at P/L = 1:40 (Figure S8 and Table S2). When H17 and the other three histidine side chains are charged ("p1, His^+ 3, 4, 11, 17"), the COM of p1 is less inserted (4.8 ± 0.2 Å) than when they are neutral (6.3 ± 0.2 Å). Deprotonating H17 while maintaining the charged state of the other three histidines allows p1 to insert deeply (6.1 ± 0.2 Å). Thus, the charge state of the single histidine present in the C-terminal region of p1 strongly influences its insertion depth.

OCD: Ability of p1 and p3 to Tilt in Bilayers. Next, we turned to studying the tilting propensity of the peptides in membranes. We used OCD to determine to a first approximation the P/L at which the peptides start reorienting in the membrane. Figure S9 displays the OCD data collected for p1 and p3 in 3:1 POPC/POPG at pH 7.4, and a hydration level similar to that used in the diffraction experiments (Table 4). At P/L = 1:150, the (almost) equal intensities at 208 and

Table 4. P/L Ratios Used to Characterize the Abilities of p1 and p3 to Reorient in, Permeabilize, and Thin Membranes

	P/L		
	dye leakage: EC_{50}	X-ray: end of abrupt thinning[a]	OCD: complete reorientation[a]
p1	1:22	1:32 (29)[b]	1:25 (40)[b]
p3	1:4	1:16 (12)[b]	1:16 (12)[b]

[a]Obtained under similar hydration conditions (approximately 10.6 waters/lipid).[84] [b]Values in parentheses represent the percent dye leakage that the peptide achieves at the specified P/L.

222 nm indicate that both peptides are α-helical and in the surface bound S-state.[16] At P/L = 1:40, the lower magnitude of the signal at 208 nm indicates that the S-state vanishes, being replaced by a tilted T-state or coexisting with a TM state that remains α-helical but is oriented perpendicular to the bilayer surface. Effects such as light scattering from the multilayered phospholipid samples can be significant at the lower wavelengths in the spectrum, preventing an unambiguous quantification of the proportion between various states.[16] However, qualitatively, the results show that at P/L = 1:25 and above, the signal at 208 nm stabilizes and almost completely vanishes in the p1 sample, indicating that p1 has completed its reorientation; that is, it has reoriented to the maximum of its tilting range, while the p3 sample is at an intermediate stage between S-state and fully reoriented. Therefore, at P/L = 1:25, when only p1 is near its threshold for 50% calcein leakage (Table 4), p1 appears to have fully tilted, while p3 has only partially reoriented in the OCD samples. In the next section, tilt values are quantified by ND and discussed.

Neutron and X-ray Diffraction: Bilayer Perturbations Caused by p1 and p3. To determine the effects of p1 and p3 on the membrane structure, we performed ND on oriented lamellar lipid mixtures of 3:1 POPC/POPG. We worked at P/L = 1:25 where the AMPs differ significantly in membrane reorientation and permeabilization capabilities, based on the OCD and dye leakage data (Table 4). As illustrated in Figure 5, variations in the neutron SLD of a bilayer projected on the z-axis, the normal to the bilayer plane, reflect the molecular composition and organization of the bilayer. Regions of low SLD are found around hydrogen-rich molecular groups (hydrocarbon chains and aqueous phase) due to the negative scattering length of hydrogen, while higher SLDs are caused by atoms enveloped in the phospholipid headgroups (phosphate, carbonyl). When we compare density profiles of neat bilayers

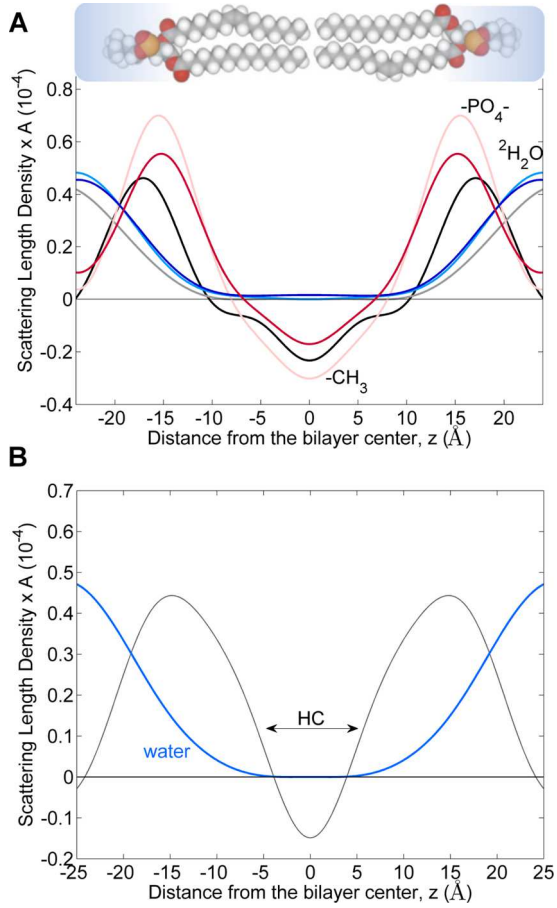

Figure 5. Neutron scattering length density profiles of bilayers and water in the presence of p1 and p3. (A) Scattering length density (SLD) profiles of a neat (lamellar) bilayer (3:1 POPC/POPG) (black), or a bilayer incorporating p1 (red) or p3 (pink), at 296 K and P/L = 1:25. The water profiles for the three samples were found by $H_2O/^2H_2O$ contrast variation: neat bilayer (gray), with p1 (dark blue), and with p3 (light blue). (B) Neutron SLD profiles for bilayer (gray) and water (^2H_2O, blue) at a high p1 concentration. Measurements were done at p1/L = 1:16, 93% relative humidity, and 296 K. The approximate extension of the hydrocarbon core (HC) is indicated.

(i.e., without peptide) with those containing p1 and p3, we find that the lipid headgroup regions broaden in the presence of the peptides. The headgroup-to-headgroup distance, estimated from the SLD maxima of the bilayer profiles (Figure 5), decreases from 34.2 Å for a neat bilayer to 30.5 and 31.1 Å for bilayers containing p1 and p3 at P/L = 1:25, respectively. The thinning and broadening of the lipid headgroups in the presence of p1 and p3 indicate that peptide partitioning in the bilayer induces reorganization of the lipid molecules.

As shown by X-ray (Figure S10) and ND (Figure 5), raising the concentration of p1 and p3 in the lipid bilayer produces a gradual change in bilayer structure and decrease in membrane thickness. This progressive change in thickness is due to an area expansion of the bilayer surface as more peptide is accommodated in the bilayer, resulting in a thinning of the hydrocarbon region at constant density that is also detected by ^2H solid-state NMR (Figure S11 and Table S7). At P/L = 1:80, the significant increase in bilayer order parameter measured by NMR reflects higher dynamics and disorder at the tip of the acyl chain. This phenomenon is often referred to

DOI: 10.1021/jacs.9b00440
J. Am. Chem. Soc. 2019, 141, 9837−9853

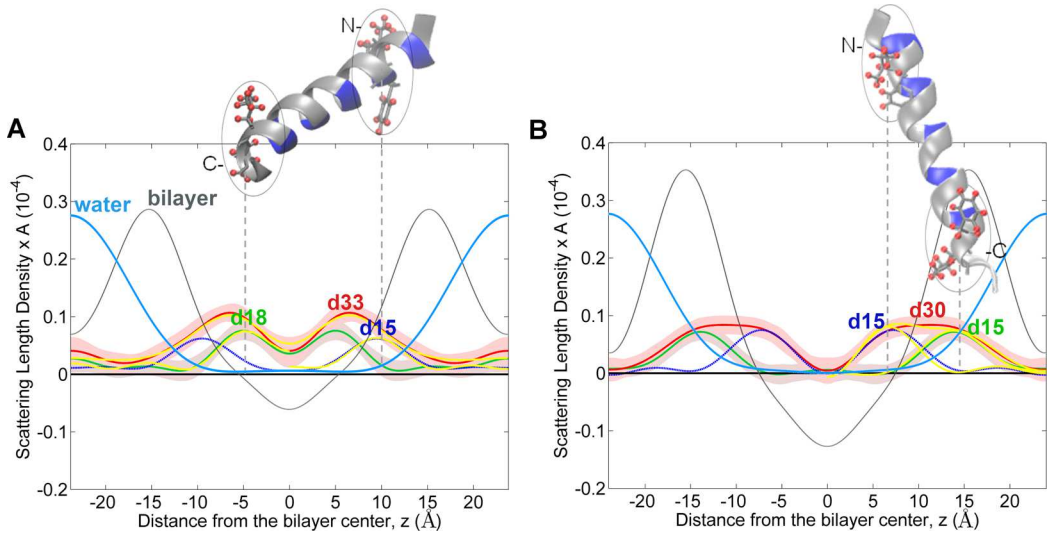

Figure 6. Analysis of the orientations and positions of p1 and p3 in bilayers. (A) Profiles of the deuterated residues of p1, projected on the *z*-axis of the bilayer: green = d18-p1 (C-terminal end) and red = d33-p1 (C- + N-terminal ends). The N-terminal deuterium profile (dark blue) was determined by deuterium difference (d15 = d33 − d18). The calculated uncertainties in the deuterium profiles are shown as pink bands (Materials and Methods). (B) Same as in (A), but for d15- and d30-p3. The overlay shows the water profiles (cyan), obtained by $H_2O/^2H_2O$ contrast variation, and the overall envelopes of the bilayer profiles with peptides in nondeuterated forms (gray). The insets (top) display the NMR structures of p1 (PDB ID 2MCU) and p3 (PDB ID 2MCW) in the conformations (bilayer orientations and positions) that best fit the restraints of the neutron profiles: red = deuterated atoms, blue = basic residues, and gray = hydrophobic residues. Only one peptide is shown, although multiple peptides partition equally on both sides of the centro-symmetric bilayer system. The profiles, which were measured at P/L = 1:25, 86% relative humidity, and 296 K, were determined on a per-lipid scale using structure factors calibrated to reflect the composition of the unit cell and without explicitly determining the area per lipid.[68]

as the basket effect because the acyl chains bend to surround the surface-bound peptide, leading to membrane thinning.[26,27] While the X-ray data show that both peptides thin the bilayer throughout a broad range of P/Ls, the more dramatic changes in bilayer thickness occur below p1/L = 1:33 = 0.030 and p3/L = 1:16 = 0.063, with p1 reducing membrane thickness significantly more than p3 in the 1:33−1:25 P/L range. Notably, the P/Ls that mark the end of the abrupt thinning agree well with the peptide concentrations needed to achieve significant tilting and initiate permeabilization (Table 4). Interestingly, the ND data collected on p1 at P/L = 1:16 (Figure 5B) show that the perturbations induced by the peptide are so dramatic that the hydrocarbon region is reduced to a small region, about 10 Å thick (versus 25 Å for neat bilayers). Because the boundary between the polar and nonpolar regions of the bilayer has almost disappeared, the bilayer has lost its original integrity under the action of p1.

Next, we employed $H_2O/^2H_2O$ exchange and deuterium contrast analysis to parse out the water distribution in bilayers with or without piscidin. As shown in Figure 5, water is mainly concentrated at the membrane surfaces, around the phospholipid headgroups, and in the space between adjacent bilayers in the lamellar samples. However, as compared to neat bilayers, the water profiles in the presence of the peptides extend further into the bilayer hydrocarbon core. Most of this water redistribution can be explained by changes in hydrogen bonding and dipolar interactions between the water, phospholipid headgroups, and peptides at the water-bilayer interface.[8] At P/L = 1:25 and 86% relative humidity, we quantified using a deuterium-based calibration method (Figure S3) that the water content (per 1 lipid) increases from 8.0 waters (± 0.1) for a neat 3:1 POPC/POPG bilayer to 8.9 waters (± 0.5) for the bilayer with p1, and 9.4 waters (± 0.1) for the bilayer with p3. We thus estimate that 23−35 water molecules per peptide are carried into the bilayer by each p1 and p3.

In previous ^{31}P solid-state NMR studies in 3:1 POPC/POPG, we detected a weak signal consistent with the merged monolayers expected for toroidal pores lined by both peptide molecules and lipid headgroups.[33] Here, given the large distortions of the bilayer and pronounced water penetration observed by ND (Figure 5B) for p1 at high peptide content, we decided to test whether toroidal pores existed in the ND samples. Water columns on the order of 15−25 Å in radii were found in samples containing magainin 2[21] and melittin[85] by in-plane ND, using $H_2O/^2H_2O$ contrast variation. These water-filled cavities were assimilated to TM toroidal pores given the presence of bent monolayers. We performed a similar type of measurement for p1 in 3:1 POPC/POPG (at p1/L = 1:12), but despite our efforts we did not detect similar TM pores. However, we detected large bilayer deformations associated with deep water penetration in the hydrocarbon region (Figure 5B and Figure S12B). How are these deformations connected to the peptide conformation?

ND with Site-Specific Deuteration: Directionality of Membrane Insertion for p1 and p3. Describing the conformations of piscidin-bilayer complexes occurring at different stages of the disruptive process is especially challenging due to the lack of high-resolution methods to simultaneously map the protein, lipid, and water components of samples. To address this, we designed an experimental strategy that combines the power of ND to map the cross-section of oriented, stacked bilayers with that of strategic peptide deuteration that can examine with subangstrom accuracy the bilayer conformation (location and orientation) of each piscidin. The p1 and p3 peptides were labeled with the stable ^2H isotope in either the C-terminal region (d18-p1 = $L19_{d10}V20_{d8}$, d15-p3 = $F19_{d5}L20_{d10}$), or both the C- and the

DOI: 10.1021/jacs.9b00440
J. Am. Chem. Soc. 2019, 141, 9837−9853

N-terminal regions (d33-p1 = $I5_{d10}F6_{d5}$ $L19_{d10}V20_{d8}$, d30-p3 = $I5_{d10}F6_{d5}$ $F19_{d5}L20_{d10}$). The contrasts between deuterium-containing and natural abundance samples arising from the higher neutron scattering length of deuterium with respect to hydrogen were used to parse out the SLD profiles of the deuterated regions (Figure 6) and obtain the distributions of the deuterated residues in the membrane.

While thermal motions prevent resolving individual deuterons, the deuterium profiles, which provide the envelope of the deuterated sites projected on the *z*-axis, still accurately determine the positions and distributions for the COM of the deuterated regions. Furthermore, without need for additional labeling, we can use the deuterium differences between (d33-p1 and d18-p1) and (d30-p3 and d15-p3), respectively, to calculate the deuterium distributions of the N-terminal region ($I5_{d10}F6_{d5}$) of each peptide (Figure 6A-B). The differences in membrane orientation between the two peptides are striking. Overall, p1 reaches deeper in the bilayer interior than p3 because the deuterium signal at $z = 0$ (bilayer center) is nonzero for p1 (Figure 6A) while it is null for p3 (Figure 6B).

Because peptides distribute equally on both sides of the membrane, we can parse out for each peptide the relative positions of its N- and C-terminal regions in the centro-symmetric system of the bilayer. The deuterium profiles for the C- and N-terminal ends of p3 show that it is slightly tilted with its N-terminus more inserted than its C-terminus. This is consistent with the partial insertion detected by OCD (Figure S9). Contrastingly, the profiles for p1 are consistent with two possible peptide orientations in the bilayer (Figure 6A and Figure S12A): (1) the p1 helix crosses the midplane of the membrane, and (2) the p1 helix is deeply buried into the bilayer hydrocarbon region, but aligned almost parallel to the bilayer surface with its C-terminal region more deeply inserted than its N-terminus. Only scenario 1 agrees with the pronounced tilting captured by OCD spectra at P/L = 1:25 (Figure S9). Accordingly, the C-terminus of p1 reaches into the hydrocarbon core of the bilayer membrane, while the N-terminus remains anchored in the lipid headgroup region. To confirm this finding and the relevance of this persistent conformation to a broader range of concentrations, we measured additional ND samples containing deuterated p1 at a higher peptide content (P/L = 1:12) (Figure S12) and found that the C-tail of p1 consistently gathers close to the middle of the hydrocarbon region.

Because the two peptides remain α-helical as they reorient in the membrane (Figure S9), we then modeled the deuterium distribution starting from the solid-state NMR high-resolution backbone structures of p1 and p3 (PDB ID nos. 2MCU and 2MCW, respectively) in 3:1 1,2-dimyristoyl-*sn*-glycero-3-phosphocholine/1,2-dimyristoyl-glycero-3-phosphoglycerol (DMPC/DMPG).[38] While POPC/POPG has acyl chains different from those of DMPC/DMPG, the 3D structures of the peptides are well conserved between lipid systems.[38] Deuterons were substituted for protons in the sites labeled in the N- and C-terminal regions (Figure 6, insets), and each deuterium was described by a Gaussian distribution, taking into account the amplitude of atomic thermal fluctuations in a bilayer (thermal B-factor). Following a methodology described previously,[70] we considered several side chain conformers and applied rigid body rotations and translations to each peptide to identify which tilt, azimuthal rotation about the helical axis, and bilayer locations fitted the ND data. Only the best fit values are reported here, based on a χ^2-minimization routine. We observed that the fit was generally better for p3 than p1 (Figure S13), possibly because the data describing p1 are affected by somewhat higher uncertainties. The values of the thermal *B*-factors for p1 and p3 at P/L = 1:25 determined from the analysis (320 and 395 Å^2, respectively) were comparable to values previously reported for lipid systems at partial hydration.[69,70,86] Using the best fits, we compared the COM positions for each set of deuterium labels (N- or C-terminal regions) relative to the bilayer center (z_{cm}) and the full-width-at-half-maximum (fwhm) of their envelopes along the *z*-axis (Figure 6). For p1, the average positions of the deuterium centroids of the N- and C-terminal ends are z^N_{cm} = 9.5 Å ± 0.5 Å (fwhm = 8.4 Å ± 0.8 Å) and z^C_{cm} = −4.8 Å ± 0.6 Å (fwhm = 7.6 Å ± 0.7 Å). For p3, these values are z^N_{cm} = 7.4 Å ± 0.4 Å (fwhm = 7.1 Å ± 0.6 Å), and z^C_{cm} = 14.2 Å ± 0.4 Å (fwhm = 9.1 Å ± 0.8 Å). Altogether, the COM of p1 is closer to the bilayer center than that of p3 by 4.6 Å, and the tilt of p1 (43.6° ± 4.2°) is much more pronounced than that of p3 (69.7° ± 1.5°) (Figure 6), accounting for its stronger smearing effect on the lipid headgroups distribution. We note that the tilt angle obtained in DMPC/DMPG (84° ± 2°)[38] is smaller than that in POPC/POPG (69.7° ± 1.5°), possibly because of the reduced packing occurring in the PO acyl chains.[60] Higher exposure of the hydrocarbon region and higher fluidity appear to result in enhanced insertion.

At a P/L = 1:12 and higher hydration, the deuterium profiles display features similar to those at P/L = 1:25, but they are more broadly distributed and noisier (Figure S12), precluding an unambiguous determination of orientation. Increased thermal and lattice disorders are expected with hydration and peptide concentration, and it is not excluded that the p1 helix experiences large orientation and position fluctuations, under these conditions. It is also possible that at the higher P/L we are close to the solubility limit of the peptide in the membrane, and some of the peptide would not be integrated in the bilayer (e.g., a fraction of the deuterium seems to be present outside the bilayer boundaries, in the aqueous phase) (Figure S12A).

SPR/EIS: Ability of p1 and p3 to Increase the Conductance of Supported Bilayers. Next, we aimed at correlating the structural perturbations of the bilayer induced by piscidin with specific types of leakage-competent defects (e.g., pores, detergents, and other nonpore mechanisms of membrane permeabilization). We conducted simultaneous SPR and EIS experiments on preformed tethered bilayer membranes (tBLM) constituted of 3:1 POPC/POPG (Figure S4). SPR provides as a function of time the total amount of material added or removed during the course of the experiment. EIS characterizes the electrical properties of the supported membrane, mainly the conductance and capacitance (thickness) of its hydrophobic, insulating part. During phase 1 of these experiments, the peptide is injected and incubated with the bilayer. In phase 2, the SPR/EIS cell is rinsed with buffer to remove loosely bound peptide molecules and equilibrate the system (Figure 7). We performed these experiments on a custom-made instrument with dual SPR and EIS capability because our aim was to correlate the electrical properties of the bilayer with the adsorption and desorption events experienced by the peptides. In contrast, the aforementioned membrane-binding kinetics experiments (Figure S5) were carried out on an automated SPR instrument capable of rapidly screening different peptide concentrations.

DOI: 10.1021/jacs.9b00440
J. Am. Chem. Soc. 2019, 141, 9837−9853

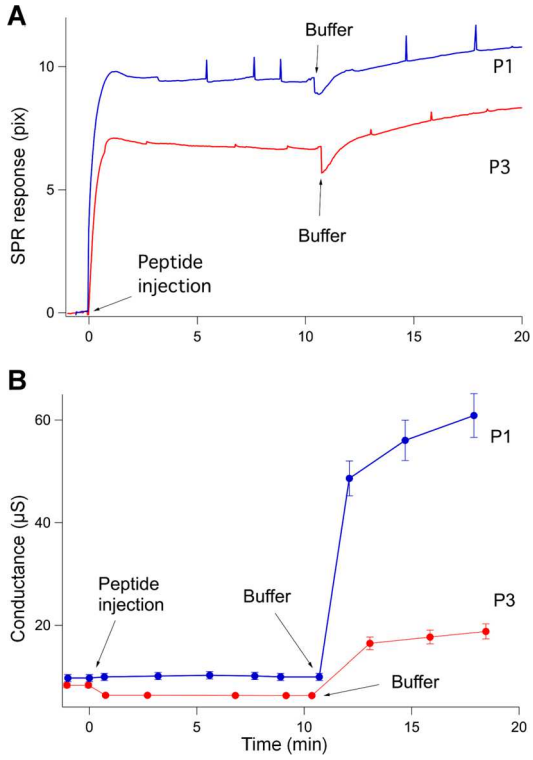

Figure 7. Simultaneous SPR and EIS measurements following the addition of p1 and p3 to supported bilayers. (A) SPR sensorgrams obtained following addition of p1 and p3 solutions to 3:1 POPC/POPG tBLMs. The SPR signal (in arbitrary units of pixels) is plotted versus time. (B) tBLM conductance changes calculated from the EIS spectra collected during and after peptide adsorption. Peptides were injected at a concentration of 3 μmol/L in HEPES buffer at pH 7.4. Arrows indicate the starting times of the peptide and buffer injections. Small spikes in the SPR sensorgram may occur at the onset of each EIS measurement. Conductance, capacitance, and SD values were calculated using a curve-fitting procedure of the EIS data to an equivalent circuit model (see Materials and Methods and Figure S4B).

Immediately after injecting p1 and p3, the SPR signal in phase 1 increases sharply for both peptides, due to a strong affinity of the cationic peptides for the bilayer, leading to rapid mass accumulation (Figure 7A). Phase 2 starts with a small decrease in SPR signal (Figure 7A), which can be attributed to desorption of loosely bound peptides from the tBLM surface. The SPR signal then quickly recovers, most likely due to structural alterations of the membrane (e.g., changes in the amount of counterions). Phase 2 is also marked by a sharp rise in the conductance of the tBLM in the presence of both peptides (Figure 7B). Thus, while loosely bound peptides are washed away at the start of the rinsing, strongly bound peptides are integrated into the bilayer, leading to the formation of defects that facilitate ion passage through the membrane.

Several important findings emerge from scrutinizing the EIS/SPR experiments. First, it is striking that the conductance does not increase until the buffer wash at the onset of phase 2. In contrast, detergents (Figure S14) and pore-forming peptides[76] increase conductance during phase 1. Second, p1 and p3 differ in both their SPR (Figure 7A) and their EIS responses (Figure 7B), with p1 being more impactful than p3 on both accounts. In particular, the higher rise in conductance obtained with p1 as compared to p3 confirms its stronger permeation ability (Figure 1 and Table 4). Third, while the conductance of the tBLM (Figure 7B) displayed no significant differences between the two peptides during phase 1, the bilayer undergoes a considerable increase in capacitance (Figure S15A), which is inversely proportional to the thickness of the tBLM (Figure S15B). Because EIS is most sensitive to changes in the thickness of the hydrocarbon region, the detected thinning is taking place in that region of the membrane, in agreement with the ND data. Under identical experimental conditions, thinning of the hydrocarbon core of the tBLM is significantly stronger with p1 (6 Å) than with p3 (2.5 Å), as described in Figure S15B. Overall, the EIS/SPR data on tBLMs show that the peptides behave differently from stable TM pores and their permeabilization effects are strongly associated with thinning of the hydrocarbon core, with p1 being significantly more effective than p3.

QCM-D: Ability of p1 and p3 to Change the Viscoelastic Properties of Supported Bilayers. To complement the SPR/EIS results that detected an increase in the conductance and capacitance of the SLB upon adding p1 and p3, we investigated the elastic (stiffness) and viscous (stress relaxation) properties of the SLB using QCM-D. With QCM-D, real-time recording of changes in crystal oscillation frequency, Δf (a reporter of mass), and energy dissipation, ΔD (a degree of viscoelasticity reporter), for various overtones (i.e., different distances from the sensor surface) provides a temporal connection between a given amount of AMP and bilayer disruption.[75,87−89] Notably, water is included in the measurements while it is not in SPR. Following the protocol from Cho et al.,[75] we formed a 3:1 POPC/POPG SLB on the silicon dioxide sensor (Δf = 25.6 ± 0.4 Hz; ΔD = (0.19 ± 0.07) × 10^{-6}) before introducing the AMPs in the flow cell (Figure S16).

Histograms for p1 (Figure 8B, left, and Figure S17A) and p3 (Figure 8B, right, and Figure S17B) at pH 7.4 present the changes occurring when Δf and ΔD are compared before peptide addition ("i" in inset of Figure 8A) and after peptide addition/buffer wash ("f" in inset of Figure 8A). These data indicate that p1 is more effective than p3 at affecting the viscoelastic properties of the SLB. Indeed, the SLB transitions from being elastic ($\Delta D < 1 \times 10^{-6}$; gray background histograms in Figure 8B and Figure S17) to viscoelastic ($\Delta D > 1 \times 10^{-6}$; white background histograms in Figures 8B and S17) at lower threshold doses of p1 (0.5 nmol) than p3 (1.0 nmol). Furthermore, the data in Figure 8C show that the Δf and ΔD changes occurring at a given peptide dose are twice larger with p1 than with p3. We note that stronger peptide-induced effects on ΔD are achieved at lower overtones, that is, near the membrane surface (Figure 8B, Figure S17, and S19), indicating that the peptide induced asymmetrical changes to the bilayer structure, possibly due to the rearrangement of the lipid headgroups, as detected by ND. Overall, the EIS/SPR and QCM-D experiments indicate that p1 and p3 disrupt supported bilayers in multifaceted ways that include increased conductance, thinning of the hydrocarbon core, rearrangement of the lipid headgroups, and transitioning from elastic to viscoelastic behavior.

■ DISCUSSION

This study compared two evolutionarily related AHs, p1 and p3. They share three histidines at their N-terminal ends, but p1 has an additional histidine that creates an amphipathic imperfection in its C-terminal region. As membrane-active

DOI: 10.1021/jacs.9b00440
J. Am. Chem. Soc. 2019, 141, 9837−9853

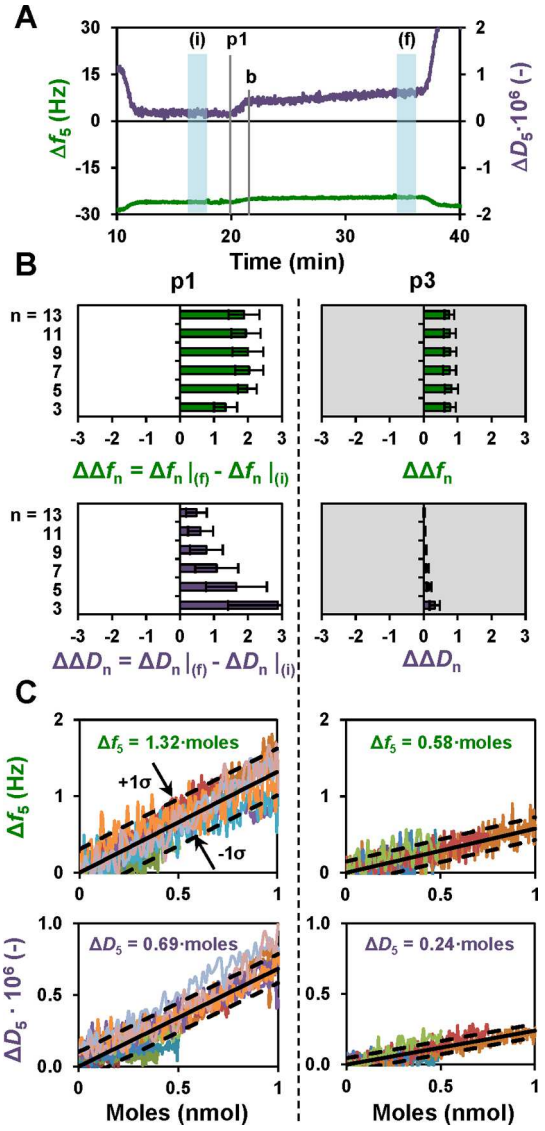

Figure 8. QCM-D analysis of piscidin–lipid interactions as a function of peptide concentration and exposure time at pH 7.4. For each QCM-D experiment, a given piscidin solution was run on a 3:1 POPC/POPG SLB over a period of time varying from 0.5 to 2 min (Figures S16 and S17). (A) Sensorgrams are shown for the data points (light blue) that were averaged to calculate $\Delta\Delta f_n$ and $\Delta\Delta D_n$ as a difference between initial (i) and final (f) values of the Δf and ΔD, respectively. The averages and SD were calculated from at least three repeats. (B) Representative histograms of Δf (green) and ΔD (purple) changes for the different overtones (from 3rd, n = 3, to 13th, n = 13) are shown using the data collected when 7.5 μmol/L AMP was flown at 100 μL/min for 1 min, corresponding to 0.75 nmol of peptide. Gray and white backgrounds indicate the validity of the Sauerbrey and Kelvin–Voigt models, respectively. (C) Averaged Δf (green, top) and ΔD (purple, bottom) for the 5th overtone versus moles (= peptide concentration [μmol/L]·volumetric flow [μL/min]·time [min]) for p1 (left) and p3 (right) interacting with the SLB. Each trace was calculated as described in Figure S18. The best linear fits (solid line) ± 1 SD (1σ, dashed line) are also included.

peptides, p1 and p3 disrupt membranes in a concentration-dependent fashion, but a molecular basis has been missing to explain why p1 is more membrane permeabilizing than p3. Our work yields a converging picture of structure–function relationships in these two peptides.

While the antimicrobial properties of piscidins have been ascribed to their ability to recognize and compromise bacterial membranes, few studies have investigated how their high, albeit differing, histidine content affects their mechanism of bilayer insertion, membrane permeabilization efficacy, and pH-behavior.[16,17,90] Mao et al. recently documented that adding a histidine at the C-terminus of Pc-Pis, a piscidin from the fish *Pseudosciaena crocea*, produced an AMP with stronger pH-resiliency and tolerance to divalent cations.[91] The significance of the neutral state of histidine for the activity of p1 and p3 revealed here is noteworthy because it highlights the importance of balanced hydrophobic and electrostatic interactions for the membrane activity of amphipathic peptides. Lower histidine and peptide charge signifies diminished opportunities for electrostatic interactions with anionic lipids. However, neutral histidines are energetically less costly to bury in the bilayer interior.[92] Furthermore, neutral bulky aromatic side chains can readily intercalate between the acyl chains of the lipids, resulting in enhanced membrane disruption.[93,94] Within a membrane environment, the neutral state of histidine could be achieved through proton transfer between the histidine side chains and lipid headgroups.[95] Even with neutral histidines, piscidin remains cationic due to multiple arginine and lysine residues. As compared to histidine, they have longer side chains with delineated hydrophobic and charged regions, allowing them to snorkel to stabilize a deep insertion.[93]

Several histidine-containing synthetic peptides that interact with membranes have been investigated under varying pH conditions, yielding results consistent with ours. For instance, Bechinger and colleagues designed histidine-rich cell-penetrating "LAH4" peptide analogues and used solution and solid-state NMR to show that pH is a key regulator of their membrane orientations.[96−100] Higher pH, which is consistent with neutral histidines, was required for cell entry by the peptides.[101,102] Interestingly, the authors showed that these histidine-rich AMPs can be more disruptive when they adopt an in-plane rather than TM orientation.[12,103] An integrated model was proposed to explain how pH can affect the charges, structures, and topologies of the peptides.[99] In another study, the same group revealed that subtle changes in cationicity at the C-terminal end of histidine-containing peptides from tree frog influence their tilt angles.[100] In another development, Koeppe and colleagues used GWALP23, an α-helical TM peptide, to investigate how the charge state of a histidine placed near the center of the bilayer affects the bilayer orientation of the peptide.[104] When the histidine was charged, the single TM state observed with a neutral histidine was dramatically destabilized. Similar results were obtained when histidines were incorporated into the TM portion of pHLIP, a pH-sensitive peptide that is rich in glutamic and aspartic residues, and is effective at targeting acidic tissues.[105] Conversely, Wiedman et al. found that the charge of histidines placed near the N- and C-terminal ends of peptides designed to form large TM pores at acidic pH did not have a major impact on their permeabilization properties.[106]

In our case, the vesicle leakage assays show that the permeabilization effects of p3, but not p1, are strongly dependent on the conserved histidines being neutral. An explanation of why p3 is so pH-sensitive, while p1 is not, emerges from combining multiple aspects of our study. As indicated by the dye leakage and OCD data and in agreement with the behaviors of other AMPs,[26,27] similar concentrations

DOI: 10.1021/jacs.9b00440
J. Am. Chem. Soc. 2019, 141, 9837−9853

of peptide are needed to permeabilize membranes and reorient the peptide in the membrane. At P/L = 1:25 and neutral pH, the NMR-monitored titrations show that the histidine side chains of p1 and p3 are neutral, while the OCD data indicate that p1 and p3 have achieved full and partial membrane reorientation, respectively. Under these conditions, ND captures p1 with its C-terminal region buried in the membrane, while p3 directs its N-terminal end toward the bilayer interior. In agreement with the high cost associated with burying charged histidine side chains in membranes,[92] our MD simulations show that p1 inserts much more deeply in the bilayer when H17, the single histidine at the extremity that directs membrane insertion, is neutral. On the basis of the titration data, this side chain prefers the neutral state even at pH 6.0. Hence, p1 inserts and remains permeabilizing at pH 6.0. However, p3 inserts through its N-terminal end, the extremity that contains all of its histidines. Because these side chains are charged at pH 6.0 (as shown by the titration data), the insertion of p3 is impeded, resulting in reduced permeabilization activity.

The AH orientation and location derived from the ND investigations offers some clues to explain how p1 peptides arrange themselves within the membrane and overcome the apparent energy penalty of transferring hydrophilic residues (T15, H17, R18, T21 found near the C-terminus) into the hydrocarbon region. Indeed, because the deuterium profile is unchanged by rotations of the peptide around the *z*-axis, it is possible that several peptide molecules and lipid headgroups cluster into a cone shape, forming an aqueous pocket lined by lipid headgroups associated with the long side chains of the charged arginine and lysine residues. Alternatively, the peptides could be arranged side-by-side, displacing the lipid molecules and leading water through the bilayer. The MD data are consistent with the conical arrangement of the peptides, although as noted in the Results, the precise arrangement varies among the defects observed.

Both the conical and the side-by-side arrangements are consistent with p1 recruiting water molecules and lipid headgroups. In a manner analogous to molecular chaperones, lipid headgroups could help stabilize the penetration of the AH across the midplane of the membrane. Because there is a strong drive to maximize hydrogen bonding in the low dielectric environment of bilayers,[2] hydrogen bonding involving multiple H17 side chains may play a key role in stabilizing the C-terminal tail of p1 in the hydrocarbon region of the bilayer. The MD simulations support this possibility as funnel-like defects transiently formed by p1 feature close histidine−histidine contacts in the membrane (Figure 4 and Figure S7 herein, and prior work[33]). This could help explain why p1 appeared to be retained more durably than p3 by bilayers in the membrane-binding kinetics experiments (Figure S5). Chen et al. also observed acute structural heterogeneity for the various inserted states adopted by synthetic AHs designed to achieve antimicrobial action via membrane poration.[34] Incorporating residues that promote intermolecular salt bridges and hydrogen bonding produced peptides that formed higher order oligomeric structures and were able to leak water across the membrane. Notably, our data, the interfacial model,[8,25] and the dynamic pore view of Chen et al.[34] support the notion that AMPs achieve membrane disruption through the formation of transient defects rather than long-lived TM pores. From this perspective, it is possible that p3 and other AMPs that cross membranes without being strongly permeabilizing form defects that are too small or short-lived to induce significant leakage.

A few features of the amino acid sequence of p1 may dictate its higher propensity for insertion in the hydrocarbon region, as compared to p3: (i) a single histidine (H17) in its C-terminal end that creates an amphipathic imperfection and provides opportunities for intermolecular contacts in the membrane to stabilize the inserted state; and (ii) a Phe-Phe motif that favors bilayer anchoring of the N-terminal end of p1, while p3 lacks this motif and has phenylalanines distributed throughout its sequence. Overall, the stronger disruptive effects of p1 are associated with the enhanced ability of its C-terminal end to insert into and desegregate the membrane regions, drawing water into the bilayer core and enhancing membrane conductance. It is possible that at peptide concentrations high enough to compromise the bilayer's insulating properties, the hydrocarbon core becomes sufficiently thin that it allows individual peptides to "snorkel" as a mechanism of transferring or translocating from one side of the bilayer to the other.

Biological membranes feature biophysical properties important to preserve in studies investigating the structures and molecular interactions of membrane-bound peptides. These characteristics include the gradient in dielectric constant and the lateral pressure profile along the bilayer normal.[50−57] Our work has examined piscidin/membrane bilayer systems under a wide range of conditions: vesicles at very high hydration (dye leakage), multilayers at full hydration (NMR);[38] multilayers at partial hydration (ND, OCD); supported bilayers (EIS, SPR, QCM-D); and, last, by MD simulations, where a single bilayer at full hydration is replicated using periodic boundary conditions. Consequently, a precise correspondence among them is not expected. For example, the surface bound average peptide orientations identified by NMR and MD differ from the tilted orientations obtained by ND and OCD. Furthermore, while the defects observed in the MD contained deeply inserted C-termini from one or two p1 (reminiscent of the average orientation observed in the ND), the MD-generated defects also contained a peptide with its N-terminus inserted. Nevertheless, there is strong consensus from all of these methods that p1 is more disruptive to the physicochemical properties of bilayers than p3; it is also more pH-resilient and able to reorient in the membrane. Most strikingly, both the ND experiments and MD simulations revealed the preferential insertion of the C-terminus of p1 and N-terminus of p3, and point at a mechanism of membrane disruption via conical defects rather than TM pores. It was essential to screen a wide range of conditions using complementary methods to fully explain the markedly different functional and structural behaviors of p1 and p3. In particular, their variations in membrane activities and pH-behaviors characterized at very high hydration (e.g., leakage assays, SPR/EIS, QCM-D) correlate with their different directionalities of membrane insertion and propensities for membrane tilting, insertion, and thinning detected at lower hydration (e.g., OCD, X-ray diffraction, and ND). Overall, our investigation highlights the value of using multiple methods and varying conditions to establish a converging view of the mechanistic steps followed by AHs as they interact dynamically with bilayers to cross and sometimes disrupt them.

On a biological level, the salient pH-resiliency of p1 suggests that this homologue plays an important role in ensuring that piscidin secretions from the mast cells of fish contain a family member fit to be active at the low pH of phagosomes. In the

DOI: 10.1021/jacs.9b00440
J. Am. Chem. Soc. 2019, 141, 9837−9853

evolutionary journey resulting in p3 being more selective than p1, p3 appears to have emerged as an AMP with lower membrane-activity strength than p1 but improved DNA-disruptive capability and selectivity for bacteria over mammalian cells.[16,37,43] Importantly, p3 cannot reach intracellular bacterial DNA without having cell-penetrating properties. Thus, the involvement of its N-terminal end in membrane insertion could reflect a salient feature used to rapidly enter cells without yielding extensive membranolytic effects, a characteristic that may have the benefit of enhancing cell selectivity.

CONCLUSION

Through this comprehensive study of p1 and p3, two homologous AMPs, we gained new insights into the molecular features that influence their permeabilization properties. The results suggest that evolutionarily related AHs use small variations in histidine content and position to slightly vary their amphipathic character, alter their directionality of membrane insertion, modulate their cell-penetrating and permeabilization properties, and achieve the required biological fitness. Altogether, our studies provide a platform of molecular features critical for not only explaining the membrane activity of AHs but also engineering efficient, "double-action" antimicrobial peptide pairs with contrasted membrane permeabilizing and DNA-disruptive properties.

ASSOCIATED CONTENT

Supporting Information

The Supporting Information is available free of charge on the ACS Publications website at DOI: 10.1021/jacs.9b00440.

Figures, tables, a list of abbreviations, and details about sample preparation and data analysis (PDF)

AUTHOR INFORMATION

Corresponding Authors

*emihailescu@ibbr.umd.edu
*belfog@rpi.edu
*mcotten@wm.edu

ORCID

Mirco Sorci: 0000-0001-6053-6702
Riqiang Fu: 0000-0003-0075-0410
Richard W. Pastor: 0000-0002-2454-5131
Linda K. Nicholson: 0000-0002-2701-1530
Georges Belfort: 0000-0002-7314-422X
Myriam L. Cotten: 0000-0002-6732-1736

Notes

The authors declare no competing financial interest.

ACKNOWLEDGMENTS

This research received support in part from the National Science Foundation (CHE-0832571 to M.L.C. and MCB-1716608 to M.L.C, M.M., and V.I.S.) and the Dreyfus Foundation (Teacher-Scholar grant to M.L.C.). We are grateful for NMR time awarded at the National High Magnetic Field Laboratory supported by the NSF Cooperative Agreement DMR-1644779, the State of Florida, and the U.S. Department of Energy. We thank Prof. David Worcester for help with the in-plane ND experiments. The investigations utilized ND facilities at the U.S. National Institute of Standards and Technology (NIST), Gaithersburg, MD. The identification of any commercial product or trade name does not imply endorsement or recommendation by NIST. R.W.P. and B.S.P. acknowledge support by the Intramural Research Program of the NIH, National Heart, Lung and Blood Institute, and the high-performance computational capabilities at the National Institutes of Health, Bethesda, MD (NHLBI LoBoS cluster). L.K.N. acknowledges support from the National Science Foundation (MCB-1615350). G.B. acknowledges endowed chair funds (RPI Fund no. 140124) and the U.S. Department of Energy, Basic Energy Sciences Division (DE-FG02-09ER16005), for funding research experiments using QCM-D and SPR.

REFERENCES

(1) McMahon, H. T.; Gallop, J. L. Membrane Curvature and Mechanisms of Dynamic Cell Membrane Remodelling. *Nature* **2005**, *438*, 590−6.
(2) Antonny, B. Mechanisms of Membrane Curvature Sensing. *Annu. Rev. Biochem.* **2011**, *80*, 101−23.
(3) Epand, R. M. Fusion Peptides and the Mechanism of Viral Fusion. *Biochim. Biophys. Acta, Biomembr.* **2003**, *1614*, 116−21.
(4) Strandberg, E.; Ulrich, A. S. Amps and Omps: Is the Folding and Bilayer Insertion of Beta-Stranded Outer Membrane Proteins Governed by the Same Biophysical Principles as for Alpha-Helical Antimicrobial Peptides? *Biochim. Biophys. Acta, Biomembr.* **2015**, *1848*, 1944−54.
(5) Zimmerberg, J.; Kozlov, M. M. How Proteins Produce Cellular Membrane Curvature. *Nat. Rev. Mol. Cell Biol.* **2006**, *7*, 9−19.
(6) Drin, G.; Casella, J. F.; Gautier, R.; Boehmer, T.; Schwartz, T. U.; Antonny, B. A General Amphipathic Alpha-Helical Motif for Sensing Membrane Curvature. *Nat. Struct. Mol. Biol.* **2007**, *14*, 138−46.
(7) Hristova, K.; Wimley, W. C.; Mishra, V. K.; Anantharamiah, G. M.; Segrest, J. P.; White, S. H. An Amphipathic Alpha-Helix at a Membrane Interface: A Structural Study Using a Novel X-Ray Diffraction Method. *J. Mol. Biol.* **1999**, *290*, 99−117.
(8) Wimley, W. C. Describing the Mechanism of Antimicrobial Peptide Action with the Interfacial Activity Model. *ACS Chem. Biol.* **2010**, *5*, 905−17.
(9) Kozlowska, J.; Vermeer, L. S.; Rogers, G. B.; Rehnnuma, N.; Amos, S. B.; Koller, G.; McArthur, M.; Bruce, K. D.; Mason, A. J. Combined Systems Approaches Reveal Highly Plastic Responses to Antimicrobial Peptide Challenge in Escherichia Coli. *PLoS Pathog.* **2014**, *10*, No. e1004104.
(10) Roversi, D.; Luca, V.; Aureli, S.; Park, Y.; Mangoni, M. L.; Stella, L. How Many Antimicrobial Peptide Molecules Kill a Bacterium? The Case of Pmap-23. *ACS Chem. Biol.* **2014**, *9*, 2003−07.
(11) Choi, H.; Yang, Z.; Weisshaar, J. C. Single-Cell, Real-Time Detection of Oxidative Stress Induced in Escherichia Coli by the Antimicrobial Peptide Cm15. *Proc. Natl. Acad. Sci. U. S. A.* **2015**, *112*, E303−10.
(12) Vogt, T. C.; Bechinger, B. The Interactions of Histidine-Containing Amphipathic Helical Peptide Antibiotics with Lipid Bilayers. The Effects of Charges and pH. *J. Biol. Chem.* **1999**, *274*, 29115−221.
(13) Pearson, C. S.; Kloos, Z.; Murray, B.; Tabe, E.; Gupta, M.; Kwak, J. H.; Karande, P.; McDonough, K. A.; Belfort, G. Combined Bioinformatic and Rational Design Approach to Develop Antimicrobial Peptides against Mycobacterium Tuberculosis. *Antimicrob. Agents Chemother.* **2016**, *60*, 2757−64.
(14) Shai, Y. Mode of Action of Membrane Active Antimicrobial Peptides. *Biopolymers* **2002**, *66*, 236−48.
(15) Fjell, C. D.; Hiss, J. A.; Hancock, R. E. W.; Schneider, G. Designing Antimicrobial Peptides: Form Follows Function. *Nat. Rev. Drug Discovery* **2012**, *11*, 37−51.
(16) Hayden, R. M.; Goldberg, G. K.; Ferguson, B. M.; Schoeneck, M. W.; Libardo, M. D. J.; Mayeux, S. E.; Shrestha, A.; Bogardus, K. A.; Hammer, J.; Pryshchep, S.; Lehman, H. K.; McCormick, M. L.;

DOI: 10.1021/jacs.9b00440
J. Am. Chem. Soc. 2019, 141, 9837−9853

Blazyk, J.; Angeles-Boza, A. M.; Fu, R.; Cotten, M. L. Complementary Effects of Host Defense Peptides Piscidin 1 and Piscidin 3 on DNA and Lipid Membranes: Biophysical Insights into Contrasting Biological Activities. *J. Phys. Chem. B* **2015**, *119*, 15235−46.
(17) Salger, S. A.; Cassady, K. R.; Reading, B. J.; Noga, E. J. A Diverse Family of Host-Defense Peptides (Piscidins) Exhibit Specialized Anti-Bacterial and Anti-Protozoal Activities in Fishes. *PLoS One* **2016**, *11*, No. e0159423.
(18) Yan, J.; Wang, K.; Dang, W.; Chen, R.; Xie, J.; Zhang, B.; Song, J.; Wang, R. Two Hits Are Better Than One: Membrane-Active and DNA Binding-Related Double-Action Mechanism of Nk-18, a Novel Antimicrobial Peptide Derived from Mammalian Nk-Lysin. *Antimicrob. Agents Chemother.* **2013**, *57*, 220−8.
(19) Nicolas, P. Multifunctional Host Defense Peptides: Intracellular-Targeting Antimicrobial Peptides. *FEBS J.* **2009**, *276*, 6483−96.
(20) Brogden, K. A. Antimicrobial Peptides: Pore Formers or Metabolic Inhibitors in Bacteria. *Nat. Rev. Microbiol.* **2005**, *3*, 239−50.
(21) Ludtke, S. J.; He, K.; Heller, W. T.; Harroun, T. A.; Yang, L.; Huang, H. W. Membrane Pores Induced by Magainin. *Biochemistry* **1996**, *35*, 13723−8.
(22) Qian, S.; Wang, W.; Yang, L.; Huang, H. W. Structure of the Alamethicin Pore Reconstructed by X-Ray Diffraction Analysis. *Biophys. J.* **2008**, *94*, 3512−22.
(23) Qian, S.; Wang, W.; Yang, L.; Huang, H. W. Structure of Transmembrane Pore Induced by Bax-Derived Peptide: Evidence for Lipidic Pores. *Proc. Natl. Acad. Sci. U. S. A.* **2008**, *105*, 17379−83.
(24) Last, N. B.; Miranker, A. D. Common Mechanism Unites Membrane Poration by Amyloid and Antimicrobial Peptides. *Proc. Natl. Acad. Sci. U. S. A.* **2013**, *110*, 6382−7.
(25) Guha, S.; Ghimire, J.; Wu, E.; Wimley, W. C. Mechanistic Landscape of Membrane-Permeabilizing Peptides. *Chem. Rev.* **2019**, *119*, 6040−85.
(26) Ouellet, M.; Bernard, G.; Voyer, N.; Auger, M. Insights on the Interactions of Synthetic Amphipathic Peptides with Model Membranes as Revealed by 31P and 2H Solid-State NMR and Infrared Spectroscopies. *Biophys. J.* **2006**, *90*, 4071−84.
(27) Balla, M. S.; Bowie, J. H.; Separovic, F. Solid-State NMR Study of Antimicrobial Peptides from Australian Frogs in Phospholipid Membranes. *Eur. Biophys. J.* **2004**, *33*, 109−16.
(28) Dathe, M.; Wieprecht, T. Structural Features of Helical Antimicrobial Peptides: Their Potential to Modulate Activity on Model Membranes and Biological Cells. *Biochim. Biophys. Acta, Biomembr.* **1999**, *1462*, 71−87.
(29) Lee, M. T.; Sun, T. L.; Hung, W. C.; Huang, H. W. Process of Inducing Pores in Membranes by Melittin. *Proc. Natl. Acad. Sci. U. S. A.* **2013**, *110*, 14243−8.
(30) Sani, M. A.; Separovic, F. How Membrane-Active Peptides Get into Lipid Membranes. *Acc. Chem. Res.* **2016**, *49*, 1130−8.
(31) Krauson, A. J.; He, J.; Wimley, W. C. Determining the Mechanism of Membrane Permeabilizing Peptides: Identification of Potent, Equilibrium Pore-Formers. *Biochim. Biophys. Acta, Biomembr.* **2012**, *1818*, 1625−32.
(32) Bechinger, B. The Smart Model: Soft Membranes Adapt and Respond, Also Transiently, in the Presence of Antimicrobial Peptides. *J. Pept. Sci.* **2015**, *21*, 346−55.
(33) Perrin, B. S.; Fu, R.; Cotten, M. L.; Pastor, R. W. Simulations of Membrane-Disrupting Peptides II: AMP Piscidin 1 Favors Surface Defects over Pores. *Biophys. J.* **2016**, *111*, 1258−66.
(34) Chen, C. H.; Starr, C. G.; Troendle, E.; Wiedman, G.; Wimley, W. C.; Ulmschneider, J. P.; Ulmschneider, M. B. Simulation-Guided Rational De Novo Design of a Small Pore-Forming Antimicrobial Peptide. *J. Am. Chem. Soc.* **2019**, *141*, 4839−48.
(35) Ulmschneider, J. P. Charged Antimicrobial Peptides Can Translocate across Membranes without Forming Channel-Like Pores. *Biophys. J.* **2017**, *113*, 73−81.
(36) Ulmschneider, J. P.; Ulmschneider, M. B. Molecular Dynamics Simulations Are Redefining Our View of Peptides Interacting with Biological Membranes. *Acc. Chem. Res.* **2018**, *51*, 1106−16.
(37) Libardo, M. D. J.; Bahar, A. A.; Ma, B.; Fu, R.; McCormick, L. E.; Zhao, J.; McCallum, S. A.; Nussinov, R.; Ren, D.; Angeles-Boza, A. M.; Cotten, M. L. Nuclease Activity Gives an Edge to Host-Defense Peptide Piscidin 3 over Piscidin 1, Rendering It More Effective against Persisters and Biofilms. *FEBS J.* **2017**, *284*, 3662−83.
(38) Perrin, B. S., Jr.; Tian, Y.; Fu, R.; Grant, C. V.; Chekmenev, E. Y.; Wieczorek, W. E.; Dao, A. E.; Hayden, R. M.; Burzynski, C. M.; Venable, R. M.; Sharma, M.; Opella, S. J.; Pastor, R. W.; Cotten, M. L. High-Resolution Structures and Orientations of Antimicrobial Peptides Piscidin 1 and Piscidin 3 in Fluid Bilayers Reveal Tilting, Kinking, and Bilayer Immersion. *J. Am. Chem. Soc.* **2014**, *136*, 3491−504.
(39) Chekmenev, E.; Vollmar, B.; Cotten, M. Can Antimicrobial Peptides Scavenge around a Cell in Less Than a Second? *Biochim. Biophys. Acta, Biomembr.* **2010**, *1798*, 228−34.
(40) Fu, R.; Gordon, E. D.; Hibbard, D. J.; Cotten, M. High Resolution Heteronuclear Correlation NMR Spectroscopy of an Antimicrobial Peptide in Aligned Bilayers at High Magnetic Field: Peptide-Water Interactions at the Water-Bilayer Interface. *J. Am. Chem. Soc.* **2009**, *131*, 10830−1.
(41) Chekmenev, E. Y.; Vollmar, B. S.; Forseth, K. T.; Manion, M. N.; Jones, S. M.; Wagner, T. J.; Endicott, R. M.; Kyriss, B. P.; Homem, L. M.; Pate, M.; He, J.; Raines, J.; Gor'kov, P. L.; Brey, W. W.; Mitchell, D. J.; Auman, A. J.; Ellard-Ivey, M.; Blazyk, J.; Cotten, M. Investigating Molecular Recognition and Biological Function at Interfaces Using Piscidins, Antimicrobial Peptides from Fish. *Biochim. Biophys. Acta, Biomembr.* **2006**, *1758*, 1359−72.
(42) Chekmenev, E. Y.; Jones, S. M.; Nikolayeva, Y. N.; Vollmar, B. S.; Wagner, T. J.; Gor'kov, P. L.; Brey, W. W.; Manion, M. N.; Daugherty, K. C.; Cotten, M. High-Field NMR Studies of Molecular Recognition and Structure-Function Relationships in Antimicrobial Piscidins at the Water-Lipid Bilayer Interface. *J. Am. Chem. Soc.* **2006**, *128*, 5308−09.
(43) Silphaduang, U.; Noga, E. J. Peptide Antibiotics in Mast Cells of Fish. *Nature* **2001**, *414*, 268−9.
(44) Dezfuli, B. S.; Pironi, F.; Giari, L.; Noga, E. J. Immunocytochemical Localization of Piscidin in Mast Cells of Infected Seabass Gill. *Fish Shellfish Immunol.* **2010**, *28*, 476−82.
(45) Sung, W. S.; Lee, J. H.; Lee, D. G. Fungicidal Effect of Piscidin on Candida Albicans: Pore Formation in Lipid Vesicles and Activity in Fungal Membranes. *Biol. Pharm. Bull.* **2008**, *31*, 1906−10.
(46) Lauth, X.; Shike, H.; Burns, J. C.; Westerman, M. E.; Ostland, V. E.; Carlberg, J. M.; Van Olst, J. C.; Nizet, V.; Taylor, S. W.; Shimizu, C.; Bulet, P. Discovery and Characterization of Two Isoforms of Moronecidin, a Novel Antimicrobial Peptide from Hybrid Striped Bass. *J. Biol. Chem.* **2002**, *277*, 5030−39.
(47) Mulero, I.; Noga, E. J.; Meseguer, J.; Garcia-Ayala, A.; Mulero, V. The Antimicrobial Peptides Piscidins Are Stored in the Granules of Professional Phagocytic Granulocytes of Fish and Are Delivered to the Bacteria-Containing Phagosome Upon Phagocytosis. *Dev. Comp. Immunol.* **2008**, *32*, 1531−8.
(48) Wang, G.; Li, X.; Wang, Z. APD2: The Updated Antimicrobial Peptide Database and Its Application in Peptide Design. *Nucleic Acids Res.* **2009**, *37*, D933−7.
(49) Lee, I. H.; Cho, Y.; Lehrer, R. I. Effects of pH and Salinity on the Antimicrobial Properties of Clavanins. *Infect. Immun.* **1997**, *65*, 2898−903.
(50) Zhou, H. X.; Cross, T. A. Influences of Membrane Mimetic Environments on Membrane Protein Structures. *Annu. Rev. Biophys.* **2013**, *42*, 361−92.
(51) Simons, K.; Sampaio, J. L. Membrane Organization and Lipid Rafts. *Cold Spring Harbor Perspect. Biol.* **2011**, *3*, No. a004697.
(52) Stern, H. A.; Feller, S. E. Calculation of the Dielectric Permittivity Profile for a Nonuniform System: Application to a Lipid Bilayer Simulation. *J. Chem. Phys.* **2003**, *118*, 3401−12.
(53) Popot, J. L.; Engelman, D. M. Membrane Protein Folding and Oligomerization: The Two-Stage Model. *Biochemistry* **1990**, *29*, 4031−7.

DOI: 10.1021/jacs.9b00440
J. Am. Chem. Soc. 2019, 141, 9837−9853

(54) Gullingsrud, J.; Schulten, K. Lipid Bilayer Pressure Profiles and Mechanosensitive Channel Gating. *Biophys. J.* **2004**, *86*, 3496−509.
(55) Cantor, R. S. Lipid Composition and the Lateral Pressure Profile in Bilayers. *Biophys. J.* **1999**, *76*, 2625−39.
(56) Belrhali, H.; Nollert, P.; Royant, A.; Menzel, C.; Rosenbusch, J. P.; Landau, E. M.; Pebay-Peyroula, E. Protein, Lipid and Water Organization in Bacteriorhodopsin Crystals: A Molecular View of the Purple Membrane at 1.9 a Resolution. *Structure* **1999**, *7*, 909−17.
(57) Kim, S.; Cross, T. A. Uniformity, Ideality, and Hydrogen Bonds in Transmembrane Alpha-Helices. *Biophys. J.* **2002**, *83*, 2084−95.
(58) Pelton, J. G.; Shi, J.; Yokota, H.; Kim, R.; Wemmer, D. E. NMR Structure of Hypothetical Protein Mg354 from Mycoplasma Genitalium. *Proteins: Struct., Funct., Genet.* **2005**, *61*, 666−8.
(59) Dawson, J.; Seckute, J.; De, S.; Schueler, S.; Oswald, A.; Nicholson, L. Elucidation of a pH-Folding Switch in the Pseudomonas Syringae Effector Protein Avrpto. *Proc. Natl. Acad. Sci. U. S. A.* **2009**, *106*, 8543−8.
(60) Perrin, B. S., Jr.; Sodt, A. J.; Cotten, M. L.; Pastor, R. W. The Curvature Induction of Surface-Bound Antimicrobial Peptides Piscidin 1 and Piscidin 3 Varies with Lipid Chain Length. *J. Membr. Biol.* **2015**, *248*, 455−67.
(61) Brooks, B. R.; III, C. L. B.; Jr, A. D. M.; Nilsson, L.; Petrella, R. J.; Roux, B.; Won, Y.; Archontis, G.; Bartels, C.; Boresch, S.; Caflisch, A.; Caves, L.; Cui, Q.; Dinner, A. R.; Feig, M.; Fischer, S.; Gao, J.; Hodoscek, M.; Im, W.; Kuczera, K.; Lazaridis, T.; Ma, J.; Ovchinnikov, V.; Paci, E.; Pastor, R. W.; Post, C. B.; Pu, J. Z.; Schaefer, M.; Tidor, B.; Venable, R. M.; Woodcock, H. L.; Wu, X.; Yang, W.; York, D. M.; Karplus, M. Charmm: The Biomolecular Simulation Program. *J. Comput. Chem.* **2009**, *30*, 1545−614.
(62) Vanommeslaeghe, K.; Hatcher, E.; Acharya, C.; Kundu, S.; Zhong, S.; Shim, J.; Darian, E.; Guvench, O.; Lopes, P.; Vorobyov, I., Jr.; A, D. M. Charmm General Force Field: A Force Field for Drug-Like Molecules Compatible with the Charmm All-Atom Additive Biological Force Field. *J. Comput. Chem.* **2009**, *31*, 671−90.
(63) Pastor, R. W.; MacKerell, A. D. Development of the Charmm Force Field for Lipids. *J. Phys. Chem. Lett.* **2011**, *2*, 1526−32.
(64) Venable, R. M.; Luo, Y.; Gawrisch, K.; Roux, B.; Pastor, R. W. Simulations of Anionic Lipid Membranes: Development of Interaction-Specific Ion Parameters and Validation Using NMR Data. *J. Phys. Chem. B* **2013**, *117*, 10183−92.
(65) Durell, S. R.; Brooks, B. R.; Ben-Naim, A. Solvent-Induced Forces between Two Hydrophilic Groups. *J. Phys. Chem.* **1994**, *98*, 2198−202.
(66) Jorgensen, W. L.; Chandrasekhar, J.; Madura, J. D. Comparison of Simple Potential Functions for Simulating Liquid Water. *J. Chem. Phys.* **1983**, *79*, 926−35.
(67) Worcester, D. L.; Franks, N. P. Structural Analysis of Hydrated Egg Lecithin and Cholesterol Bilayers. II. Neutrol Diffraction. *J. Mol. Biol.* **1976**, *100*, 359−78.
(68) Wiener, M. C.; King, G. I.; White, S. H. Structure of a Fluid Dioleoylphosphatidylcholine Bilayer Determined by Joint Refinement of X-Ray and Neutron Diffraction Data. I. Scaling of Neutron Data and the Distributions of Double Bonds and Water. *Biophys. J.* **1991**, *60*, 568−76.
(69) Buldt, G.; Gally, H. U.; Seelig, A.; Seelig, J.; Zaccai, G. Neutron Diffraction Studies on Selectively Deuterated Phospholipid Bilayers. *Nature* **1978**, *271*, 182−4.
(70) Mihailescu, M.; Krepkiy, D.; Milescu, M.; Gawrisch, K.; Swartz, K. J.; White, S. Structural Interactions of a Voltage Sensor Toxin with Lipid Membranes. *Proc. Natl. Acad. Sci. U. S. A.* **2014**, *111*, E5463−70.
(71) Press, W. H.; Flannery, B. P.; Teukolsky, S. A.; Vetterling, W. T. *Numerical Recipes. The Art of Scientific Computing*; Cambridge University Press: Cambridge, UK, 1986.
(72) Scott, D. R.; Silin, V.; Nanda, H. Reconstitution of Functionalized Transmembrane Domains of Receptor Proteins into Biomimetic Membranes. *Langmuir* **2015**, *31*, 9115−24.
(73) McGillivray, D. J.; Valincius, G.; Vanderah, D. J.; Febo-Ayala, W.; Woodward, J. T.; Heinrich, F.; Kasianowicz, J. J.; Losche, M. Molecular-Scale Structural and Functional Characterization of Sparsely Tethered Bilayer Lipid Membranes. *Biointerphases* **2007**, *2*, 21−33.
(74) Vanderah, D. J.; Parr, T.; Silin, V.; Meuse, C. W.; Gates, R. S.; La, H.; Valincius, G. Isostructural Self-Assembled Monolayers. 2. Methyl 1-(3-Mercaptopropyl)-Oligo(Ethylene Oxide)S. *Langmuir* **2004**, *20*, 1311−6.
(75) Cho, N. J.; Frank, C. W.; Kasemo, B.; Hook, F. Quartz Crystal Microbalance with Dissipation Monitoring of Supported Lipid Bilayers on Various Substrates. *Nat. Protoc.* **2010**, *5*, 1096−106.
(76) Briand, E.; Zach, M.; Svedhem, S.; Kasemo, B.; Petronis, S. Combined QCM-D and EIS Study of Supported Lipid Bilayer Formation and Interaction with Pore-Forming Peptides. *Analyst* **2010**, *135*, 343−50.
(77) Huang, H. W. Action of Antimicrobial Peptides: Two-State Model. *Biochemistry* **2000**, *39*, 8347−52.
(78) Oregioni, A.; Stieglitz, B.; Kelly, G.; Rittinger, K.; Frenkiel, T. Determination of the pKa of the N-Terminal Amino Group of Ubiquitin by NMR. *Sci. Rep.* **2017**, *7*, 43748.
(79) Liao, S. M.; Du, Q. S.; Meng, J. Z.; Pang, Z. W.; Huang, R. B. The Multiple Roles of Histidine in Protein Interactions. *Chem. Cent. J.* **2013**, *7*, 44.
(80) Campagna, S.; Saint, N.; Molle, G.; Aumelas, A. Structure and Mechanism of Action of the Antimicrobial Peptide Piscidin. *Biochemistry* **2007**, *46*, 1771−8.
(81) Lee, S. A.; Kim, Y. K.; Lim, S. S.; Zhu, W. L.; Ko, H.; Shin, S. Y.; Hahm, K. S.; Kim, Y. Solution Structure and Cell Selectivity of Piscidin 1 and Its Analogues. *Biochemistry* **2007**, *46*, 3653−63.
(82) Chipot, C.; Dehez, F.; Schnell, J. R.; Zitzmann, N.; Pebay-Peyroula, E.; Catoire, L. J.; Miroux, B.; Kunji, E. R. S.; Veglia, G.; Cross, T. A.; Schanda, P. Perturbations of Native Membrane Protein Structure in Alkyl Phosphocholine Detergents: A Critical Assessment of NMR and Biophysical Studies. *Chem. Rev.* **2018**, *118*, 3559−607.
(83) Venable, R. M.; Brown, F. L. H.; Pastor, R. W. Mechanical Properties of Lipid Bilayers from Molecular Dynamics Simulation. *Chem. Phys. Lipids* **2015**, *192*, 60−74.
(84) Krepkiy, D.; Mihailescu, M.; Freites, J. A.; Schow, E. V.; Worcester, D. L.; Gawrisch, K.; Tobias, D. J.; White, S. H.; Swartz, K. J. Structure and Hydration of Membranes Embedded with Voltage-Sensing Domains. *Nature* **2009**, *462*, 473−9.
(85) Yang, L.; Harroun, T. A.; Weiss, T. M.; Ding, L.; Huang, H. W. Barrel-Stave Model or Toroidal Model? A Case Study on Melittin Pores. *Biophys. J.* **2001**, *81*, 1475−85.
(86) Mihailescu, M.; Vaswani, R. G.; Jardon-Valadez, E.; Castro-Roman, F.; Freites, J. A.; Worcester, D. L.; Chamberlin, A. R.; Tobias, D. J.; White, S. H. Acyl-Chain Methyl Distributions of Liquid-Ordered and -Disordered Membranes. *Biophys. J.* **2011**, *100*, 1455−62.
(87) Nielsen, S. B.; Otzen, D. E. Impact of the Antimicrobial Peptide Novicidin on Membrane Structure and Integrity. *J. Colloid Interface Sci.* **2010**, *345*, 248−56.
(88) McCubbin, G. A.; Praporski, S.; Piantavigna, S.; Knappe, D.; Hoffmann, R.; Bowie, J. H.; Separovic, F.; Martin, L. L. QCM-D Fingerprinting of Membrane-Active Peptides. *Eur. Biophys. J.* **2011**, *40*, 437−46.
(89) Murray, B.; Pearson, C. S.; Aranjo, A.; Cherupalla, D.; Belfort, G. Mechanism of Four De Novo Designed Antimicrobial Peptides. *J. Biol. Chem.* **2016**, *291*, 25706−15.
(90) Narayana, J. L.; Huang, H. N.; Wu, C. J.; Chen, J. Y. Efficacy of the Antimicrobial Peptide TP4 against Helicobacter Pylori Infection: In Vitro Membrane Perturbation Via Micellization and in Vivo Suppression of Host Immune Responses in a Mouse Model. *Oncotarget* **2015**, *6*, 12936−54.
(91) Mao, Y.; Niu, S.; Xu, X.; Wang, J.; Su, Y.; Wu, Y.; Zhong, S. The Effect of an Adding Histidine on Biological Activity and Stability of Pc-Pis from Pseudosciaena Crocea. *PLoS One* **2013**, *8*, No. e83268.
(92) Wimley, W. C.; White, S. H. Experimentally Determined Hydrophobicity Scale for Proteins at Membrane Interfaces. *Nat. Struct. Mol. Biol.* **1996**, *3*, 842−8.

DOI: 10.1021/jacs.9b00440
J. Am. Chem. Soc. 2019, 141, 9837−9853

(93) Saravanan, R.; Li, X.; Lim, K.; Mohanram, H.; Peng, L.; Mishra, B.; Basu, A.; Lee, J. M.; Bhattacharjya, S.; Leong, S. S. Design of Short Membrane Selective Antimicrobial Peptides Containing Tryptophan and Arginine Residues for Improved Activity, Salt-Resistance, and Biocompatibility. *Biotechnol. Bioeng.* **2014**, *111*, 37−49.
(94) Kozic, M.; Fox, S. J.; Thomas, J. M.; Verma, C. S.; Rigden, D. J. Large Scale Ab Initio Modeling of Structurally Uncharacterized Antimicrobial Peptides Reveals Known and Novel Folds. *Proteins: Struct., Funct., Genet.* **2018**, *86*, 548−65.
(95) Bondar, A.-N.; White, S. H. Hydrogen Bond Dynamics in Membrane Protein Function. *Biochim. Biophys. Acta, Biomembr.* **2012**, *1818*, 942−50.
(96) Bechinger, B. Towards Membrane Protein Design: pH-Sensitive Topology of Histidine-Containing Polypeptides. *J. Mol. Biol.* **1996**, *263*, 768−75.
(97) Mason, A. J.; Chotimah, I. N. H.; Bertani, P.; Bechinger, B. A Spectroscopic Study of the Membrane Interaction of the Antimicrobial Peptide Pleurocidin. *Mol. Membr. Biol.* **2006**, *23*, 185−94.
(98) Aisenbrey, C.; Kinder, R.; Goormaghtigh, E.; Ruysschaert, J. M.; Bechinger, B. Interactions Involved in the Realignment of Membrane-Associated Helices: An Investigation Using Oriented Solid-State NMR and Attenuated Total Reflection Fourier Transform Infrared Spectroscopies. *J. Biol. Chem.* **2006**, *281*, 7708−16.
(99) Georgescu, J.; Munhoz, V. H.; Bechinger, B. NMR Structures of the Histidine-Rich Peptide LAH4 in Micellar Environments: Membrane Insertion, pH-Dependent Mode of Antimicrobial Action, and DNA Transfection. *Biophys. J.* **2010**, *99*, 2507−15.
(100) Resende, J. M.; Verly, R. M.; Aisenbrey, C.; Cesar, A.; Bertani, P.; Pilo-Veloso, D.; Bechinger, B. Membrane Interactions of Phylloseptin-1, −2, and −3 Peptides by Oriented Solid-State NMR Spectroscopy. *Biophys. J.* **2014**, *107*, 901−11.
(101) Vermeer, L. S.; Hamon, L.; Schirer, A.; Schoup, M.; Cosette, J.; Majdoul, S.; Pastre, D.; Stockholm, D.; Holic, N.; Hellwig, P.; Galy, A.; Fenard, D.; Bechinger, B. Vectofusin-1, a Potent Peptidic Enhancer of Viral Gene Transfer Forms pH-Dependent Alpha-Helical Nanofibrils, Concentrating Viral Particles. *Acta Biomater.* **2017**, *64*, 259−68.
(102) Kichler, A.; Mason, A. J.; Marquette, A.; Bechinger, B. Histidine-Rich Cationic Amphipathic Peptides for Plasmid DNA and siRNA Delivery. *Methods Mol. Biol.* **2013**, *948*, 85−103.
(103) Farrotti, A.; Bocchinfuso, G.; Palleschi, A.; Rosato, N.; Salnikov, E. S.; Voievoda, N.; Bechinger, B.; Stella, L. Molecular Dynamics Methods to Predict Peptide Locations in Membranes: LAH4 as a Stringent Test Case. *Biochim. Biophys. Acta, Biomembr.* **2015**, *1848*, 581−92.
(104) Martfeld, A. N.; Greathouse, D. V.; Koeppe, R. E. 2nd, Ionization Properties of Histidine Residues in the Lipid Bilayer Membrane Environment. *J. Biol. Chem.* **2016**, *291*, 19146−56.
(105) Barrera, F. N.; Weerakkody, D.; Anderson, M.; Andreev, O. A.; Reshetnyak, Y. K.; Engelman, D. M. Roles of Carboxyl Groups in the Transmembrane Insertion of Peptides. *J. Mol. Biol.* **2011**, *413*, 359−71.
(106) Wiedman, G.; Kim, S. Y.; Zapata-Mercado, E.; Wimley, W. C.; Hristova, K. pH-Triggered, Macromolecule-Sized Poration of Lipid Bilayers by Synthetically Evolved Peptides. *J. Am. Chem. Soc.* **2017**, *139*, 937−45.

DOI: 10.1021/jacs.9b00440
J. Am. Chem. Soc. 2019, 141, 9837−9853